Recognition of Human Iris Patterns for Biometric Identification

Libor Masek

Abstract

A biometric system provides automatic identification of an individual based on a unique feature or characteristic possessed by the individual. Iris recognition is regarded as the most reliable and accurate biometric identification system available. Most commercial iris recognition systems use patented algorithms developed by Daugman, and these algorithms are able to produce perfect recognition rates. However, published results have usually been produced under favourable conditions, and there have been no independent trials of the technology.

The work presented in this thesis involved developing an 'open-source' iris recognition system in order to verify both the uniqueness of the human iris and also its performance as a biometric. For determining the recognition performance of the system two databases of digitised greyscale eye images were used.

The iris recognition system consists of an automatic segmentation system that is based on the Hough transform, and is able to localise the circular iris and pupil region, occluding eyelids and eyelashes, and reflections. The extracted iris region was then normalised into a rectangular block with constant dimensions to account for imaging inconsistencies. Finally, the phase data from 1D Log-Gabor filters was extracted and quantised to four levels to encode the unique pattern of the iris into a bit-wise biometric template.

The Hamming distance was employed for classification of iris templates, and two templates were found to match if a test of statistical independence was failed. The system performed with perfect recognition on a set of 75 eye images; however, tests on another set of 624 images resulted in false accept and false reject rates of 0.005% and 0.238% respectively. Therefore, iris recognition is shown to be a reliable and accurate biometric technology.

Acknowledgements

Contents

Chapter 1

Introduction

1.1 Biometric Technology

A biometric system provides automatic recognition of an individual based on some sort of unique feature or characteristic possessed by the individual. Biometric systems have been developed based on fingerprints, facial features, voice, hand geometry, handwriting, the retina [1], and the one presented in this thesis, the iris.

Biometric systems work by first capturing a sample of the feature, such as recording a digital sound signal for voice recognition, or taking a digital colour image for face recognition. The sample is then transformed using some sort of mathematical function into a biometric template. The biometric template will provide a normalised, efficient and highly discriminating representation of the feature, which can then be objectively compared with other templates in order to determine identity. Most biometric systems allow two modes of operation. An enrolment mode for adding templates to a database, and an identification mode, where a template is created for an individual and then a match is searched for in the database of pre-enrolled templates.

A good biometric is characterised by use of a feature that is; highly unique – so that the chance of any two people having the same characteristic will be minimal, stable – so that the feature does not change over time, and be easily captured – in order to provide convenience to the user, and prevent misrepresentation of the feature.

1.2 The Human Iris

The iris is a thin circular diaphragm, which lies between the cornea and the lens of the human eye. A front-on view of the iris is shown in Figure 1.1. The iris is perforated close to its centre by a circular aperture known as the pupil. The function of the iris is to control the amount of light entering through the pupil, and this is done by the sphincter and the dilator muscles, which adjust the size of the pupil. The average diameter of the iris is 12 mm, and the pupil size can vary from 10% to 80% of the iris diameter [2].

The iris consists of a number of layers, the lowest is the epithelium layer, which contains dense pigmentation cells. The stromal layer lies above the epithelium layer, and contains blood vessels, pigment cells and the two iris muscles. The density of stromal pigmentation determines the colour of the iris. The externally visible surface of the multi-layered iris contains two zones, which often differ in colour [3]. An outer ciliary zone and an inner pupillary zone, and these two zones are divided by the collarette – which appears as a zigzag pattern.

1
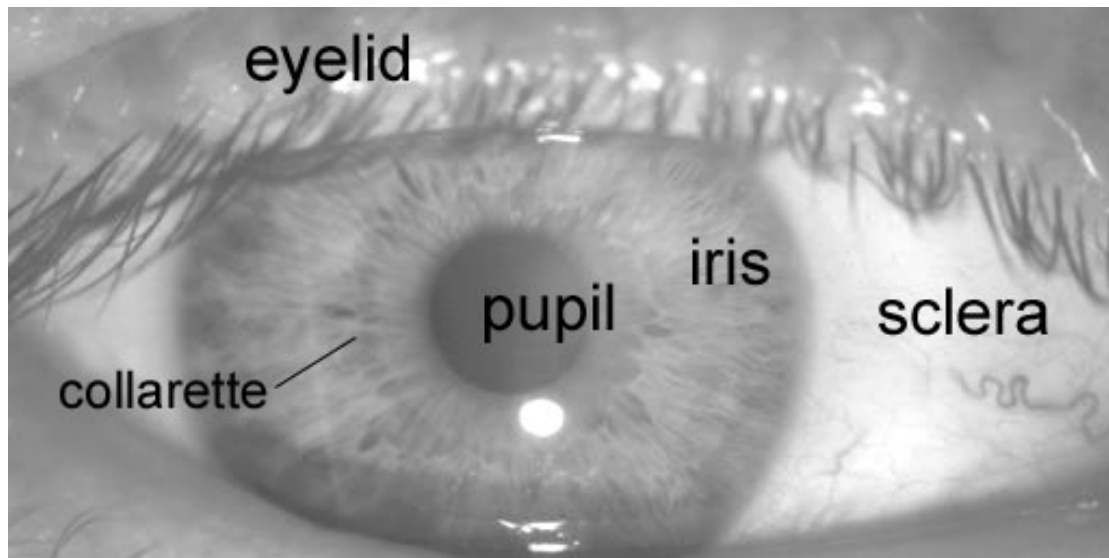
Figure 1.1 – A front-on view of the human eye.

Formation of the iris begins during the third month of embryonic life [3]. The unique pattern on the surface of the iris is formed during the first year of life, and pigmentation of the stroma takes place for the first few years. Formation of the unique patterns of the iris is random and not related to any genetic factors [4]. The only characteristic that is dependent on genetics is the pigmentation of the iris, which determines its colour. Due to the epigenetic nature of iris patterns, the two eyes of an individual contain completely independent iris patterns, and identical twins possess uncorrelated iris patterns. For further details on the anatomy of the human eye consult the book by Wolff [3].

1.3   Iris Recognition

The iris is an externally visible, yet protected organ whose unique epigenetic pattern remains stable throughout adult life. These characteristics make it very attractive for use as a biometric for identifying individuals. Image processing techniques can be employed to extract the unique iris pattern from a digitised image of the eye, and encode it into a biometric template, which can be stored in a database. This biometric template contains an objective mathematical representation of the unique information stored in the iris, and allows comparisons to be made between templates. When a subject wishes to be identified by an iris recognition system, their eye is first photographed, and then a template created for their iris region. This template is then compared with the other templates stored in a database until either a matching template is found and the subject is identified, or no match is found and the subject remains unidentified.

Although prototype systems had been proposed earlier, it was not until the early nineties that Cambridge researcher, John Daugman, implemented a working automated iris recognition system [1][2]. The Daugman system is patented [5] and the rights are now owned by the company Iridian Technologies. Even though the Daugman system is the most successful and most well known, many other systems have been developed. The most notable include the systems of Wildes et al. [7][4],

Boles and Boashash [8], Lim et al. [9], and Noh et al. [10]. The algorithms by Lim et al. are used in the iris recognition system developed by the Evermedia and Senex companies. Also, the Noh et al. algorithm is used in the 'IRIS2000' system, sold by IriTech. These are, apart from the Daugman system, the only other known commercial implementations.

The Daugman system has been tested under numerous studies, all reporting a zero failure rate. The Daugman system is claimed to be able to perfectly identify an individual, given millions of possibilities. The prototype system by Wildes et al. also reports flawless performance with 520 iris images [7], and the Lim et al. system attains a recognition rate of 98.4% with a database of around 6,000 eye images.

Compared with other biometric technologies, such as face, speech and finger recognition, iris recognition can easily be considered as the most reliable form of biometric technology [1]. However, there have been no independent trials of the technology, and source code for systems is not available. Also, there is a lack of publicly available datasets for testing and research, and the test results published have usually been produced using carefully imaged irises under favourable conditions.

1.4   Objective

The objective will be to implement an open-source iris recognition system in order to verify the claimed performance of the technology. The development tool used will be MATLAB®, and emphasis will be only on the software for performing recognition, and not hardware for capturing an eye image. A rapid application development (RAD) approach will be employed in order to produce results quickly. MATLAB® provides an excellent RAD environment, with its image processing toolbox, and high level programming methodology. To test the system, two data sets of eye images will be used as inputs; a database of 756 greyscale eye images courtesy of The Chinese Academy of Sciences – Institute of Automation (CASIA) [13], and a database of 120 digital greyscale images courtesy of the Lion's Eye Institute (LEI) [14].

The system is to be composed of a number of sub-systems, which correspond to each stage of iris recognition. These stages are segmentation – locating the iris region in an eye image, normalisation – creating a dimensionally consistent representation of the iris region, and feature encoding – creating a template containing only the most discriminating features of the iris. The input to the system will be an eye image, and the output will be an iris template, which will provide a mathematical representation of the iris region. For an overview of the components of the system see Appendix B.

Chapter 2

Segmentation

2.1 Overview

The first stage of iris recognition is to isolate the actual iris region in a digital eye image. The iris region, shown in Figure 1.1, can be approximated by two circles, one for the iris/sclera boundary and another, interior to the first, for the iris/pupil boundary. The eyelids and eyelashes normally occlude the upper and lower parts of the iris region. Also, specular reflections can occur within the iris region corrupting the iris pattern. A technique is required to isolate and exclude these artefacts as well as locating the circular iris region.

The success of segmentation depends on the imaging quality of eye images. Images in the CASIA iris database [13] do not contain specular reflections due to the use of near infra-red light for illumination. However, the images in the LEI database [14] contain these specular reflections, which are caused by imaging under natural light. Also, persons with darkly pigmented irises will present very low contrast between the pupil and iris region if imaged under natural light, making segmentation more difficult. The segmentation stage is critical to the success of an iris recognition system, since data that is falsely represented as iris pattern data will corrupt the biometric templates generated, resulting in poor recognition rates.

2.2 Literature Review

2.2.1 Hough Transform

The Hough transform is a standard computer vision algorithm that can be used to determine the parameters of simple geometric objects, such as lines and circles, present in an image. The circular Hough transform can be employed to deduce the radius and centre coordinates of the pupil and iris regions. An automatic segmentation algorithm based on the circular Hough transform is employed by Wildes et al. [7], Kong and Zhang [15], Tisse et al. [12], and Ma et al. [16]. Firstly, an edge map is generated by calculating the first derivatives of intensity values in an eye image and then thresholding the result. From the edge map, votes are cast in Hough space for the parameters of circles passing through each edge point. These parameters are the centre coordinates x_c and y_c, and the radius r, which are able to define any circle according to the equation

$$x_c^2 + y_c^2 - r^2 = 0 \qquad\qquad \textbf{(2.1)}$$

A maximum point in the Hough space will correspond to the radius and centre coordinates of the circle best defined by the edge points. Wildes et al. and Kong and Zhang also make use of the parabolic Hough transform to detect the eyelids, approximating the upper and lower eyelids with parabolic arcs, which are represented as;

$$(-(x-h_j)\sin\theta_j + (y-k_j)\cos\theta_j)^2 = a_j((x-h_j)\cos\theta_j + (y-k_j)\sin\theta_j) \quad \textbf{(2.2)}$$

where a_j controls the curvature, (h_j, k_j) is the peak of the parabola and θ_j is the angle of rotation relative to the x-axis.

In performing the preceding edge detection step, Wildes et al. bias the derivatives in the horizontal direction for detecting the eyelids, and in the vertical direction for detecting the outer circular boundary of the iris, this is illustrated in Figure 2.1. The motivation for this is that the eyelids are usually horizontally aligned, and also the eyelid edge map will corrupt the circular iris boundary edge map if using all gradient data. Taking only the vertical gradients for locating the iris boundary will reduce influence of the eyelids when performing circular Hough transform, and not all of the edge pixels defining the circle are required for successful localisation. Not only does this make circle localisation more accurate, it also makes it more efficient, since there are less edge points to cast votes in the Hough space.

original   edge map   horizontal   vertical
                                    edge map   edge map

a   **b**   **c**   **d**
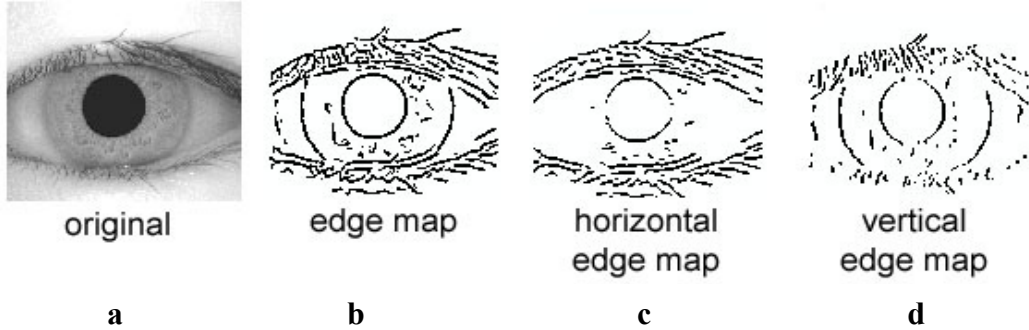
Figure 2.1– a) an eye image (020_2_1 from the CASIA database) **b)** corresponding edge map **c)** edge map with only horizontal gradients **d)** edge map with only vertical gradients.

There are a number of problems with the Hough transform method. First of all, it requires threshold values to be chosen for edge detection, and this may result in critical edge points being removed, resulting in failure to detect circles/arcs. Secondly, the Hough transform is computationally intensive due to its 'brute-force' approach, and thus may not be suitable for real time applications.

2.2.2 Daugman's Integro-differential Operator

Daugman makes use of an integro-differential operator for locating the circular iris and pupil regions, and also the arcs of the upper and lower eyelids. The integro-differential operator is defined as

$$\max_{(r,x_p,y_o)} \left| G_\sigma(r) * \frac{\partial}{\partial r} \oint_{r,x_o,y_0} \frac{I(x,y)}{2\pi r} ds \right| \qquad (2.3)$$

where *I(x,y)* is the eye image, *r* is the radius to search for, $G_\sigma(r)$ is a Gaussian smoothing function, and *s* is the contour of the circle given by *r, x₀, y₀*. The operator searches for the circular path where there is maximum change in pixel values, by varying the radius and centre *x* and *y* position of the circular contour. The operator is applied iteratively with the amount of smoothing progressively reduced in order to attain precise localisation. Eyelids are localised in a similar manner, with the path of contour integration changed from circular to an arc.

The integro-differential can be seen as a variation of the Hough transform, since it too makes use of first derivatives of the image and performs a search to find geometric parameters. Since it works with raw derivative information, it does not suffer from the thresholding problems of the Hough transform. However, the algorithm can fail where there is noise in the eye image, such as from reflections, since it works only on a local scale.

2.2.3 Active Contour Models

Ritter et al. [17] make use of active contour models for localising the pupil in eye images. Active contours respond to pre-set internal and external forces by deforming internally or moving across an image until equilibrium is reached. The contour contains a number of vertices, whose positions are changed by two opposing forces, an internal force, which is dependent on the desired characteristics, and an external force, which is dependent on the image. Each vertex is moved between time t and t + 1 by

$$v_i(t+1) = v_i(t) + F_i(t) + G_i(t) \qquad (2.4)$$

where F_i is the internal force, G_i is the external force and v_i is the position of vertex *i*. For localisation of the pupil region, the internal forces are calibrated so that the contour forms a globally expanding discrete circle. The external forces are usually found using the edge information. In order to improve accuracy Ritter et al. use the variance image, rather than the edge image.

A point interior to the pupil is located from a variance image and then a discrete circular active contour (DCAC) is created with this point as its centre. The DCAC is then moved under the influence of internal and external forces until it reaches equilibrium, and the pupil is localised.

2.2.4 Eyelash and Noise Detection

Kong and Zhang [15] present a method for eyelash detection, where eyelashes are treated as belonging to two types, separable eyelashes, which are isolated in the image, and multiple eyelashes, which are bunched together and overlap in the eye

image. Separable eyelashes are detected using 1D Gabor filters, since the convolution of a separable eyelash with the Gaussian smoothing function results in a low output value. Thus, if a resultant point is smaller than a threshold, it is noted that this point belongs to an eyelash. Multiple eyelashes are detected using the variance of intensity. If the variance of intensity values in a small window is lower than a threshold, the centre of the window is considered as a point in an eyelash. The Kong and Zhang model also makes use of connective criterion, so that each point in an eyelash should connect to another point in an eyelash or to an eyelid. Specular reflections along the eye image are detected using thresholding, since the intensity values at these regions will be higher than at any other regions in the image.

2.3   Implementation

It was decided to use circular Hough transform for detecting the iris and pupil boundaries. This involves first employing Canny edge detection to generate an edge map. Gradients were biased in the vertical direction for the outer iris/sclera boundary, as suggested by Wildes et al. [4]. Vertical and horizontal gradients were weighted equally for the inner iris/pupil boundary. A modified version of Kovesi's Canny edge detection MATLAB® function [22] was implemented, which allowed for weighting of the gradients.

The range of radius values to search for was set manually, depending on the database used. For the CASIA database, values of the iris radius range from 90 to 150 pixels, while the pupil radius ranges from 28 to 75 pixels. In order to make the circle detection process more efficient and accurate, the Hough transform for the iris/sclera boundary was performed first, then the Hough transform for the iris/pupil boundary was performed within the iris region, instead of the whole eye region, since the pupil is always within the iris region. After this process was complete, six parameters are stored, the radius, and x and y centre coordinates for both circles.

Eyelids were isolated by first fitting a line to the upper and lower eyelid using the linear Hough transform. A second horizontal line is then drawn, which intersects with the first line at the iris edge that is closest to the pupil. This process is illustrated in Figure 2.2 and is done for both the top and bottom eyelids. The second horizontal line allows maximum isolation of eyelid regions. Canny edge detection is used to create an edge map, and only horizontal gradient information is taken. The linear Hough transform is implemented using the MATLAB® Radon transform, which is a form of the Hough transform. If the maximum in Hough space is lower than a set threshold, then no line is fitted, since this corresponds to non-occluding eyelids. Also, the lines are restricted to lie exterior to the pupil region, and interior to the iris region. A linear Hough transform has the advantage over its parabolic version, in that there are less parameters to deduce, making the process less computationally demanding.
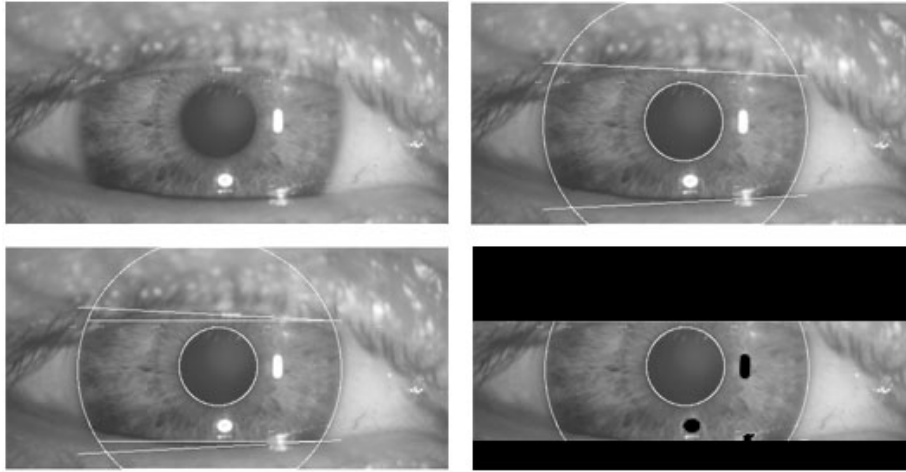
Figure 2.2 - Stages of segmentation with eye image 'pi201b' from the LEI database **Top left**) original eye image **Top right**) two circles overlayed for iris and pupil boundaries, and two lines for top and bottom eyelid **Bottom left**) horizontal lines are drawn for each eyelid from the lowest/highest point of the fitted line **Bottom right**) probable eyelid and specular reflection areas isolated (black areas)

For isolating eyelashes in the CASIA database a simple thresholding technique was used, since analysis reveals that eyelashes are quite dark when compared with the rest of the eye image. Analysis of the LEI eye images shows that thresholding to detect eyelashes would not be successful. Although, the eyelashes are quite dark compared with the surrounding eyelid region, areas of the iris region are equally dark due to the imaging conditions. Therefore thresholding to isolate eyelashes would also remove important iris region features, making this technique infeasible. However, eyelash occlusion is not very prominent so no technique was implemented to isolate eyelashes in the LEI database.

The LEI database also required isolation of specular reflections. This was implemented, again, using thresholding, since reflection areas are characterised by high pixel values close to 255. For the eyelid, eyelash, and reflection detection process, the coordinates of any of these noise areas are marked using the MATLAB® NaN type, so that intensity values at these points are not misrepresented as iris region data.

2.4   Results

The automatic segmentation model proved to be successful. The CASIA database provided good segmentation, since those eye images had been taken specifically for iris recognition research and boundaries of iris pupil and sclera were clearly distinguished. For the CASIA database, the segmentation technique managed to correctly segment the iris region from 624 out of 756 eye images, which corresponds to a success rate of around 83%. The LEI images proved problematic and the segmentation process correctly identified iris and pupil boundaries for only 75 out of 120 eye images, which corresponds to a success rate of around 62%.

The problem images had small intensity differences between the iris region and the pupil region as shown in Figure 2.3. One problem faced with the implementation was

that it required different parameters to be set for each database. These parameters were the radius of iris and pupil to search for, and threshold values for creating edge maps. However, for installations of iris recognition systems, these parameters would only need to be set once, since the camera hardware, imaging distance, and lighting conditions would usually remain the same.
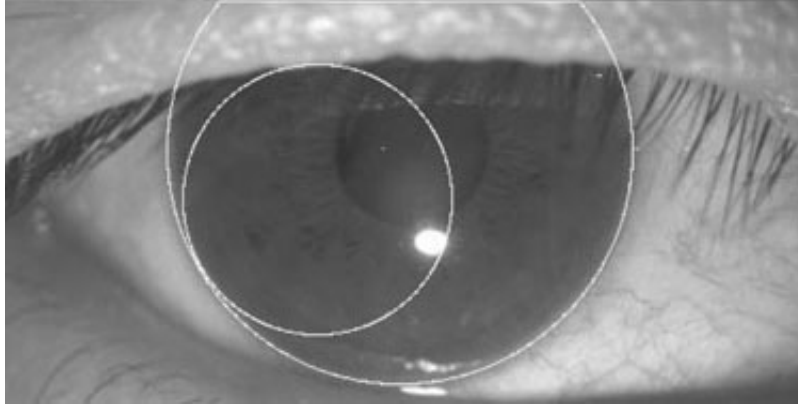
Figure 2.3 – An example where segmentation fails for the LEI database. Here there is little contrast between pupil and iris regions, so Canny edge detection fails to find the edges of the pupil border.

The eyelid detection system also proved quite successful, and managed to isolate most occluding eyelid regions. One problem was that it would sometimes isolate too much of the iris region, which could make the recognition process less accurate, since there is less iris information. However, this is preferred over including too much of the iris region, if there is a high chance it would also include undetected eyelash and eyelid regions.

The eyelash detection system implemented for the CASIA database also proved to be successful in isolating most of the eyelashes occurring within the iris region as shown in Figure 2.4.
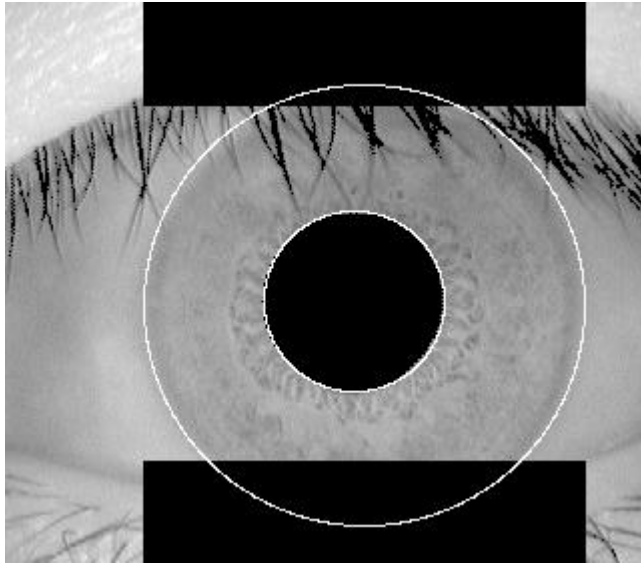
Figure 2.4 – The eyelash detection technique, eyelash regions are detected using thresholding and denoted as black. Note that some lighter eyelashes are not detected. Image '021_1_2' from the CASIA database.

A slight problem was that areas where the eyelashes were light, such as at the tips, were not detected. However, these undetected areas were small when compared with the size of the iris region. Isolation of specular reflections from eye images in the LEI database also proved to be successful and numerous examples of their isolation are shown in Figure 2.6.
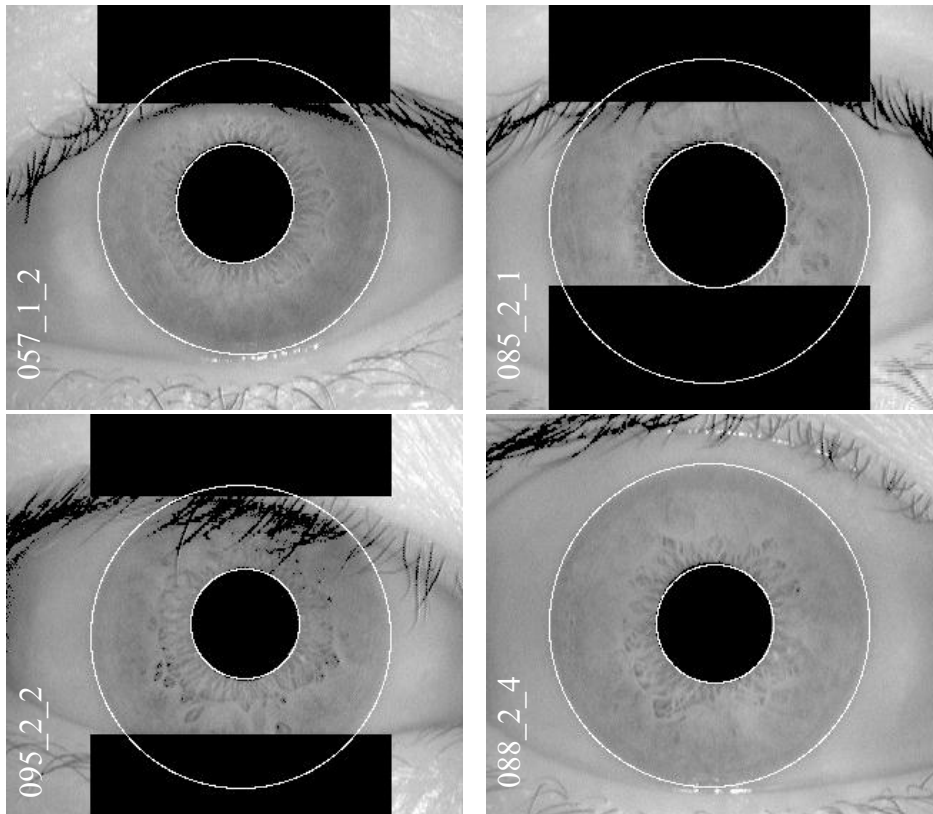
Figure 2.5 – Automatic segmentation of various images from the CASIA database. Black regions denote detected eyelid and eyelash regions.
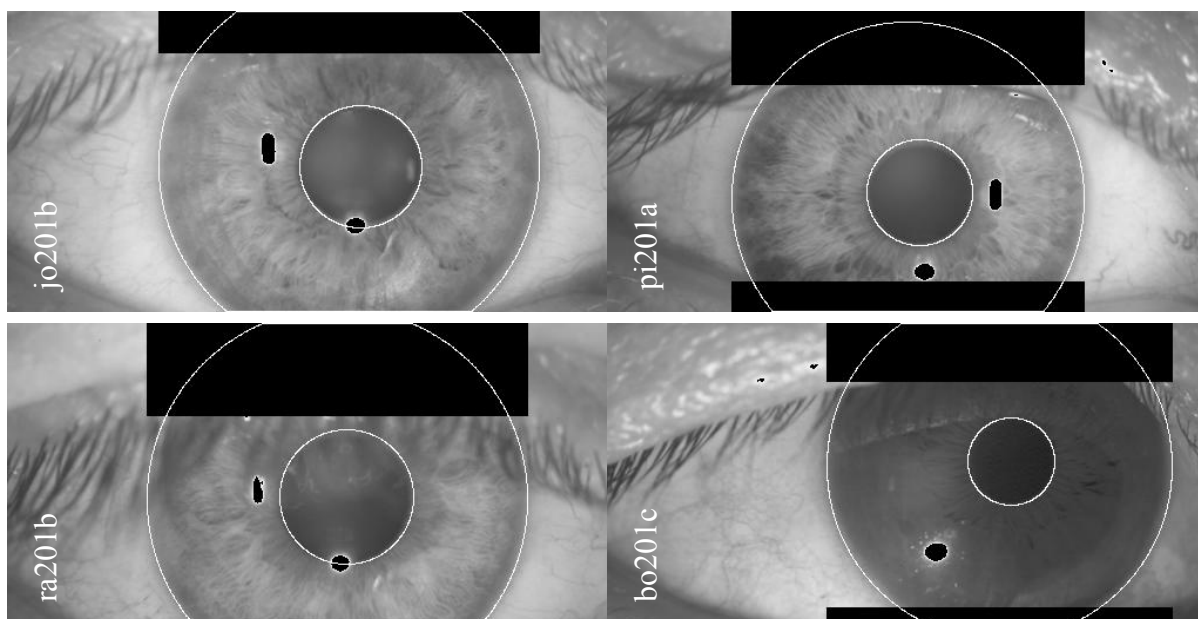
Figure 2.6 – Automatic segmentation of various images from the 'LEI' database, note the undetected occluding eyelashes in 'ra201b' and 'bo201c'. Black regions denote detected eyelids and specular reflections.

Chapter 3

Normalisation

3.1 Overview

Once the iris region is successfully segmented from an eye image, the next stage is to transform the iris region so that it has fixed dimensions in order to allow comparisons. The dimensional inconsistencies between eye images are mainly due to the stretching of the iris caused by pupil dilation from varying levels of illumination. Other sources of inconsistency include, varying imaging distance, rotation of the camera, head tilt, and rotation of the eye within the eye socket. The normalisation process will produce iris regions, which have the same constant dimensions, so that two photographs of the same iris under different conditions will have characteristic features at the same spatial location.

Another point of note is that the pupil region is not always concentric within the iris region, and is usually slightly nasal [2]. This must be taken into account if trying to normalise the 'doughnut' shaped iris region to have constant radius.

3.2 Literature Review

3.2.1 Daugman's Rubber Sheet Model

The homogenous rubber sheet model devised by Daugman [1] remaps each point within the iris region to a pair of polar coordinates (r,θ) where r is on the interval [0,1] and θ is angle [0,2π].
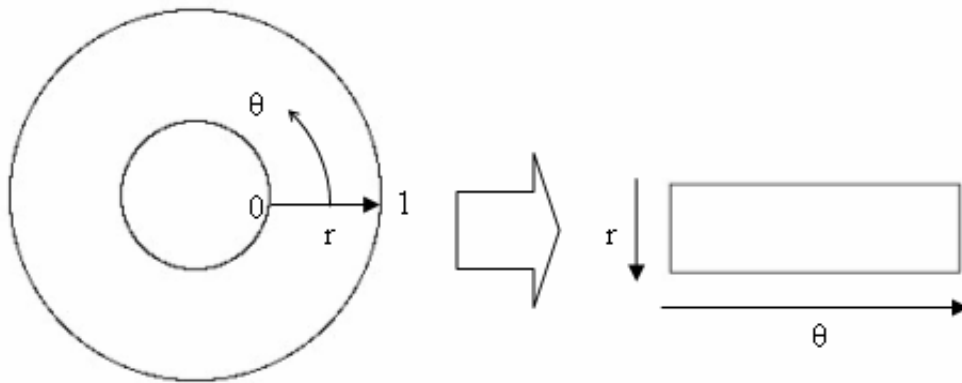
Figure 3.1 – Daugman's rubber sheet model.

The remapping of the iris region from *(x,y)* Cartesian coordinates to the normalised non-concentric polar representation is modelled as

$$I(x(r,\theta), y(r,\theta)) \rightarrow I(r,\theta) \qquad (3.1)$$

with

$$x(r,\theta) = (1-r)x_p(\theta) + rx_l(\theta)$$
$$y(r,\theta) = (1-r)y_p(\theta) + ry_l(\theta)$$

where *I(x,y)* is the iris region image, *(x,y)* are the original Cartesian coordinates, *(r,θ)* are the corresponding normalised polar coordinates, and x_p, y_p and x_l, y_l are the coordinates of the pupil and iris boundaries along the *θ* direction. The rubber sheet model takes into account pupil dilation and size inconsistencies in order to produce a normalised representation with constant dimensions. In this way the iris region is modelled as a flexible rubber sheet anchored at the iris boundary with the pupil centre as the reference point.

Even though the homogenous rubber sheet model accounts for pupil dilation, imaging distance and non-concentric pupil displacement, it does not compensate for rotational inconsistencies. In the Daugman system, rotation is accounted for during matching by shifting the iris templates in the *θ* direction until two iris templates are aligned.

3.2.2 Image Registration

The Wildes et al. system employs an image registration technique, which geometrically warps a newly acquired image, $I_a(x,y)$ into alignment with a selected database image $I_d(x,y)$ [4]. When choosing a mapping function $(u(x,y), v(x,y))$ to transform the original coordinates, the image intensity values of the new image are made to be close to those of corresponding points in the reference image. The mapping function must be chosen so as to minimise

$$\int_x\int_y (I_d(x,y) - I_a(x-u, y-v))^2 \, dxdy \qquad (3.2)$$

while being constrained to capture a similarity transformation of image coordinates (x,y) to (x',y'), that is

$$\begin{pmatrix} x' \\ y' \end{pmatrix} = \begin{pmatrix} x \\ y \end{pmatrix} - sR(\phi)\begin{pmatrix} x \\ y \end{pmatrix} \qquad (3.3)$$

with *s* a scaling factor and $R(\phi)$ a matrix representing rotation by ϕ. In implementation, given a pair of iris images I_a and I_d, the warping parameters s and ϕ are recovered via an iterative minimisation procedure [4].

3.2.3 Virtual Circles

In the Boles [8] system, iris images are first scaled to have constant diameter so that when comparing two images, one is considered as the reference image. This works differently to the other techniques, since normalisation is not performed until attempting to match two iris regions, rather than performing normalisation and saving the result for later comparisons. Once the two irises have the same dimensions, features are extracted from the iris region by storing the intensity values along virtual concentric circles, with origin at the centre of the pupil. A normalisation resolution is selected, so that the number of data points extracted from each iris is the same. This is essentially the same as Daugman's rubber sheet model, however scaling is at match time, and is relative to the comparing iris region, rather than scaling to some constant dimensions. Also, it is not mentioned by Boles, how rotational invariance is obtained.

3.3 Implementation

For normalisation of iris regions a technique based on Daugman's rubber sheet model was employed. The centre of the pupil was considered as the reference point, and radial vectors pass through the iris region, as shown in Figure 3.2. A number of data points are selected along each radial line and this is defined as the radial resolution. The number of radial lines going around the iris region is defined as the angular resolution. Since the pupil can be non-concentric to the iris, a remapping formula is needed to rescale points depending on the angle around the circle. This is given by

$$r' = \sqrt{\alpha}\beta \pm \sqrt{\alpha\beta^2 - \alpha - r_I^2} \qquad\qquad (3.4)$$

with

$$\alpha = o_x^2 + o_y^2$$

$$\beta = \cos\left(\pi - \arctan\left(\frac{o_y}{o_x}\right) - \theta\right)$$

where displacement of the centre of the pupil relative to the centre of the iris is given by o_x, o_y, and r' is the distance between the edge of the pupil and edge of the iris at an angle, θ around the region, and r_I is the radius of the iris. The remapping formula first gives the radius of the iris region 'doughnut' as a function of the angle θ.

A constant number of points are chosen along each radial line, so that a constant number of radial data points are taken, irrespective of how narrow or wide the radius is at a particular angle. The normalised pattern was created by backtracking to find the Cartesian coordinates of data points from the radial and angular position in the normalised pattern. From the 'doughnut' iris region, normalisation produces a 2D array with horizontal dimensions of angular resolution and vertical dimensions of radial resolution. Another 2D array was created for marking reflections, eyelashes, and eyelids detected in the segmentation stage. In order to prevent non-iris region data from corrupting the normalised representation, data points which occur along the

pupil border or the iris border are discarded. As in Daugman's rubber sheet model, removing rotational inconsistencies is performed at the matching stage and will be discussed in the next chapter.
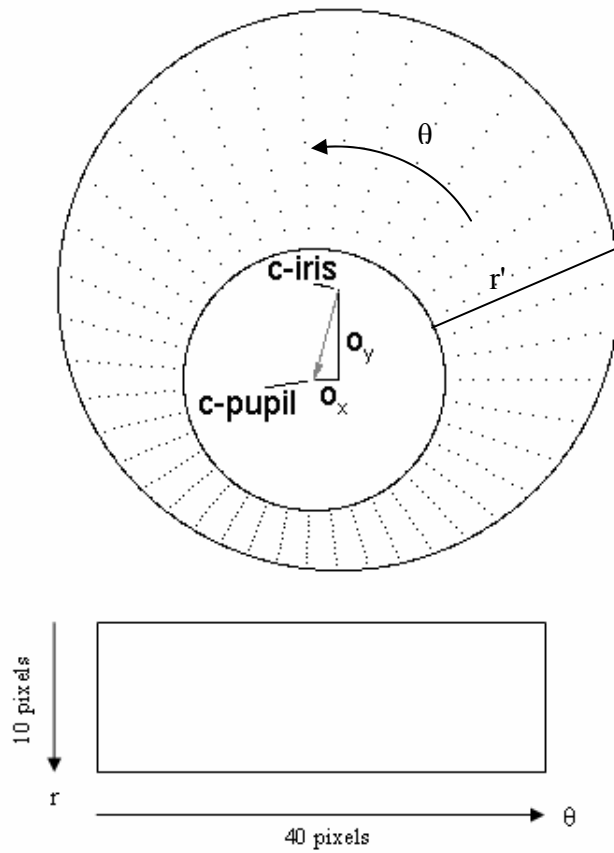
Figure 3.2 – Outline of the normalisation process with radial resolution of 10 pixels, and angular resolution of 40 pixels. Pupil displacement relative to the iris centre is exaggerated for illustration purposes.

3.4 Results

The normalisation process proved to be successful and some results are shown in Figure 3.3. However, the normalisation process was not able to perfectly reconstruct the same pattern from images with varying amounts of pupil dilation, since deformation of the iris results in small changes of its surface patterns.
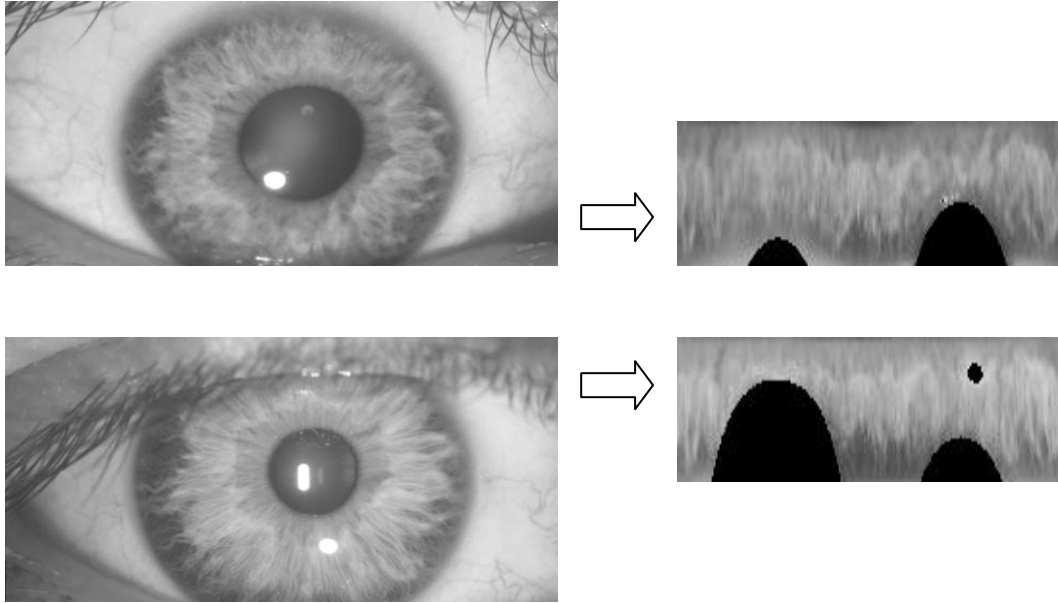
Figure 3.3 – Illustration of the normalisation process for two images of the same iris taken under varying conditions. Top image 'am201b', bottom image 'am201g' from the LEI database.

Normalisation of two eye images of the same iris is shown in Figure 3.3. The pupil is smaller in the bottom image, however the normalisation process is able to rescale the iris region so that it has constant dimension. In this example, the rectangular representation is constructed from 10,000 data points in each iris region. Note that rotational inconsistencies have not been accounted for by the normalisation process, and the two normalised patterns are slightly misaligned in the horizontal (angular) direction. Rotational inconsistencies will be accounted for in the matching stage.

Chapter 4

Feature Encoding and Matching

4.1 Overview

In order to provide accurate recognition of individuals, the most discriminating information present in an iris pattern must be extracted. Only the significant features of the iris must be encoded so that comparisons between templates can be made. Most iris recognition systems make use of a band pass decomposition of the iris image to create a biometric template.

The template that is generated in the feature encoding process will also need a corresponding matching metric, which gives a measure of similarity between two iris templates. This metric should give one range of values when comparing templates generated from the same eye, known as intra-class comparisons, and another range of values when comparing templates created from different irises, known as inter-class comparisons. These two cases should give distinct and separate values, so that a decision can be made with high confidence as to whether two templates are from the same iris, or from two different irises.

4.2 Literature Review of Feature Encoding Algorithms

4.2.1 Wavelet Encoding

Wavelets can be used to decompose the data in the iris region into components that appear at different resolutions. Wavelets have the advantage over traditional Fourier transform in that the frequency data is localised, allowing features which occur at the same position and resolution to be matched up. A number of wavelet filters, also called a bank of wavelets, is applied to the 2D iris region, one for each resolution with each wavelet a scaled version of some basis function. The output of applying the wavelets is then encoded in order to provide a compact and discriminating representation of the iris pattern.

4.2.2 Gabor Filters

Gabor filters are able to provide optimum conjoint representation of a signal in space and spatial frequency. A Gabor filter is constructed by modulating a sine/cosine wave with a Gaussian. This is able to provide the optimum conjoint localisation in both space and frequency, since a sine wave is perfectly localised in frequency, but not localised in space. Modulation of the sine with a Gaussian provides localisation in space, though with loss of localisation in frequency. Decomposition of a signal is accomplished using a quadrature pair of Gabor filters, with a real part specified by a cosine modulated by a Gaussian, and an imaginary part specified by a sine modulated

by a Gaussian. The real and imaginary filters are also known as the even symmetric and odd symmetric components respectively.

The centre frequency of the filter is specified by the frequency of the sine/cosine wave, and the bandwidth of the filter is specified by the width of the Gaussian.

Daugman makes uses of a 2D version of Gabor filters [1] in order to encode iris pattern data. A 2D Gabor filter over the an image domain *(x,y)* is represented as

$$G(x,y) = e^{-\pi[(x-x_0)^2/\alpha^2+(y-y_0)^2/\beta^2]}e^{-2\pi i[u_0(x-x_0)+v_0(y-y_0)]} \qquad \textbf{(4.1)}$$

where *(x₀,y₀)* specify position in the image, *(α,β)* specify the effective width and length, and *(u₀, v₀)* specify modulation, which has spatial frequency $\omega_0 = \sqrt{u_0^2 + v_0^2}$. The odd symmetric and even symmetric 2D Gabor filters are shown in Figure 4.1.
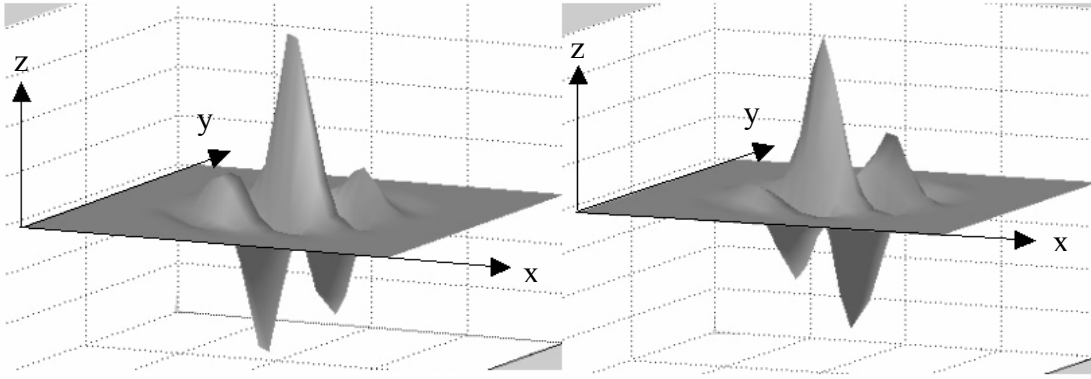
Figure 4.1 – A quadrature pair of 2D Gabor filters **left)** real component or even symmetric filter characterised by a cosine modulated by a Gaussian **right)** imaginary component or odd symmetric filter characterised by a sine modulated by a Gaussian.

Daugman demodulates the output of the Gabor filters in order to compress the data. This is done by quantising the phase information into four levels, for each possible quadrant in the complex plane. It has been shown by Oppenheim and Lim [23] that phase information, rather than amplitude information provides the most significant information within an image. Taking only the phase will allow encoding of discriminating information in the iris, while discarding redundant information such as illumination, which is represented by the amplitude component.

These four levels are represented using two bits of data, so each pixel in the normalised iris pattern corresponds to two bits of data in the iris template. A total of 2,048 bits are calculated for the template, and an equal number of masking bits are generated in order to mask out corrupted regions within the iris. This creates a compact 256-byte template, which allows for efficient storage and comparison of irises. The Daugman system makes use of polar coordinates for normalisation, therefore in polar form the filters are given as

$$H(r,\theta) = e^{-i\omega(\theta-\theta_0)} e^{-(r-r_0)^2/\alpha^2} e^{-i(\theta-\theta_0)^2/\beta^2} \qquad \textbf{(4.2)}$$

where *(α,β)* are the same as in Equation 4.1 and *(r₀, θ₀)* specify the centre frequency of the filter.

The demodulation and phase Quantisation process can be represented as

$$h_{\{Re,Im\}} = \text{sgn}_{\{Re,Im\}} \iint_{\rho\,\phi} I(\rho,\phi) e^{-i\omega(\theta_0-\phi)} e^{-(r_0-\rho)^2/\alpha^2} e^{-(\theta_0-\phi)^2/\beta^2} \rho\, d\rho\, d\phi \qquad \textbf{(4.3)}$$

where $h_{\{Re,\,Im\}}$ can be regarded as a complex valued bit whose real and imaginary components are dependent on the sign of the 2D integral, and $I(\rho,\phi)$ is the raw iris image in a dimensionless polar coordinate system. For a detailed study of 2D Gabor wavelets see [26].

4.2.3 Log-Gabor Filters

A disadvantage of the Gabor filter is that the even symmetric filter will have a DC component whenever the bandwidth is larger than one octave [20]. However, zero DC component can be obtained for any bandwidth by using a Gabor filter which is Gaussian on a logarithmic scale, this is known as the Log-Gabor filter. The frequency response of a Log-Gabor filter is given as;

$$G(f) = \exp\left(\frac{-(\log(f/f_0))^2}{2(\log(\sigma/f_0))^2} \right) \qquad \textbf{(4.4)}$$

where f_0 represents the centre frequency, and σ gives the bandwidth of the filter. Details of the Log-Gabor filter are examined by Field [20].

4.2.4 Zero-crossings of the 1D wavelet

Boles and Boashash [8] make use of 1D wavelets for encoding iris pattern data. The mother wavelet is defined as the second derivative of a smoothing function *θ(x)*.

$$\psi(x) = \frac{d^2\theta(x)}{dx^2} \qquad \textbf{(4.5)}$$

The zero crossings of dyadic scales of these filters are then used to encode features. The wavelet transform of a signal *f(x)* at scale *s* and position *x* is given by

$$W_s f(x) = f * \left(s^2 \frac{d^2\theta(x)}{dx^2} \right)(x)$$
$$\qquad\qquad \textbf{(4.6)}$$
$$= s^2 \frac{d^2}{dx^2}(f * \theta_s)(x)$$

where

$$\theta_s = (1/s)\theta(x/s)$$

$W_s f(x)$ is proportional to the second derivative of *f(x)* smoothed by $\theta_s(x)$, and the zero crossings of the transform correspond to points of inflection in *f*θₛ(x)*. The motivation for this technique is that zero-crossings correspond to significant features with the iris region.

4.2.5 Haar Wavelet

Lim et al. [9] also use the wavelet transform to extract features from the iris region. Both the Gabor transform and the Haar wavlet are considered as the mother wavelet. From multi-dimensionally filtering, a feature vector with 87 dimensions is computed. Since each dimension has a real value ranging from -1.0 to +1.0, the feature vector is sign quantised so that any positive value is represented by 1, and negative value as 0. This results in a compact biometric template consisting of only 87 bits.

Lim et al. compare the use of Gabor transform and Haar wavelet transform, and show that the recognition rate of Haar wavelet transform is slightly better than Gabor transform by 0.9%.

4.2.6 Laplacian of Gaussian Filters

In order to encode features, the Wildes et al. system decomposes the iris region by application of Laplacian of Gaussian filters to the iris region image. The filters are given as

$$\nabla G = -\frac{1}{\pi\sigma^4}\left(1 - \frac{\rho^2}{2\sigma^2}\right)e^{-\rho^2/2\sigma^2} \qquad \textbf{(4.7)}$$

where σ is the standard deviation of the Gaussian and ρ is the radial distance of a point from the centre of the filter.

The filtered image is represented as a Laplacian pyramid which is able to compress the data, so that only significant data remains. Details of Laplacian Pyramids are presented by Burt and Adelson [24]. A Laplacian pyramid is constructed with four different resolution levels in order to generate a compact iris template.

4.3 Literature Review of Matching Algorithms

4.3.1 Hamming distance

The Hamming distance gives a measure of how many bits are the same between two bit patterns. Using the Hamming distance of two bit patterns, a decision can be made

as to whether the two patterns were generated from different irises or from the same one.

In comparing the bit patterns *X* and *Y*, the Hamming distance, *HD*, is defined as the sum of disagreeing bits (sum of the exclusive-OR between *X* and *Y*) over *N*, the total number of bits in the bit pattern.

$$HD = \frac{1}{N} \sum_{j=1}^{N} X_j (XOR) Y_j \qquad\qquad \textbf{(4.8)}$$

Since an individual iris region contains features with high degrees of freedom, each iris region will produce a bit-pattern which is independent to that produced by another iris, on the other hand, two iris codes produced from the same iris will be highly correlated.

If two bits patterns are completely independent, such as iris templates generated from different irises, the Hamming distance between the two patterns should equal 0.5. This occurs because independence implies the two bit patterns will be totally random, so there is 0.5 chance of setting any bit to 1, and vice versa. Therefore, half of the bits will agree and half will disagree between the two patterns. If two patterns are derived from the same iris, the Hamming distance between them will be close to 0.0, since they are highly correlated and the bits should agree between the two iris codes.

The Hamming distance is the matching metric employed by Daugman, and calculation of the Hamming distance is taken only with bits that are generated from the actual iris region.

4.3.2 Weighted Euclidean Distance

The weighted Euclidean distance (WED) can be used to compare two templates, especially if the template is composed of integer values. The weighting Euclidean distance gives a measure of how similar a collection of values are between two templates. This metric is employed by Zhu et al. [11] and is specified as

$$WED(k) = \sum_{i=1}^{N} \frac{(f_i - f_i^{(k)})^2}{(\delta_i^{(k)})^2} \qquad\qquad \textbf{(4.9)}$$

where f_i is the ith feature of the unknown iris, and $f_i^{(k)}$ is the ith feature of iris template, *k*, and $\delta_i^{(k)}$ is the standard deviation of the ith feature in iris template *k*. The unknown iris template is found to match iris template *k*, when *WED* is a minimum at *k*.

4.3.3 Normalised Correlation

Wildes et al. make use of normalised correlation between the acquired and database representation for goodness of match. This is represented as

$$\frac{\sum_{i=1}^{n}\sum_{j=1}^{m}(p_1[i,j]-\mu_1)(p_2[i,j]-\mu_2)}{nm\sigma_1\sigma_2}$$

(4.10)

where p_1 and p_2 are two images of size $n_x m$, μ_1 and σ_1 are the mean and standard deviation of p_1, and μ_2 and σ_2 are the mean and standard deviation of p_2.

Normalised correlation is advantageous over standard correlation, since it is able to account for local variations in image intensity that corrupt the standard correlation calculation.

4.4   Implementation

4.4.1 Feature Encoding

Feature encoding was implemented by convolving the normalised iris pattern with 1D Log-Gabor wavelets. The 2D normalised pattern is broken up into a number of 1D signals, and then these 1D signals are convolved with 1D Gabor wavelets. The rows of the 2D normalised pattern are taken as the 1D signal, each row corresponds to a circular ring on the iris region. The angular direction is taken rather than the radial one, which corresponds to columns of the normalised pattern, since maximum independence occurs in the angular direction.

The intensity values at known noise areas in the normalised pattern are set to the average intensity of surrounding pixels to prevent influence of noise in the output of the filtering. The output of filtering is then phase quantised to four levels using the Daugman method [1], with each filter producing two bits of data for each phasor. The output of phase quantisation is chosen to be a grey code, so that when going from one quadrant to another, only 1 bit changes. This will minimise the number of bits disagreeing, if say two intra-class patterns are slightly misaligned and thus will provide more accurate recognition. The feature encoding process is illustrated in Figure 4.2.

The encoding process produces a bitwise template containing a number of bits of information, and a corresponding noise mask which corresponds to corrupt areas within the iris pattern, and marks bits in the template as corrupt. Since the phase information will be meaningless at regions where the amplitude is zero, these regions are also marked in the noise mask. The total number of bits in the template will be the angular resolution times the radial resolution, times 2, times the number of filters used. The number of filters, their centre frequencies and parameters of the modulating Gaussian function in order to achieve the best recognition rate will be discussed in the next chapter.

Original 1D signal

Intensity

Position

Even symmetric

Odd symmetric

1D Gabor Filter

Real response

Imaginary response

Response

Response

Phase Quantisation

Im

[0,1]

[1,1]

Re

[0,0]

[1,0]

Iris Template

01 00 00 10 11 11 01 01 00 10 10 11 11 01 01 00 10 10 11 01 01 01 01 01 00
10 10 01 11 00 01 11 10 11 10 10 00 10 01 10 00 11 01 10 11 00 01 01 11 10
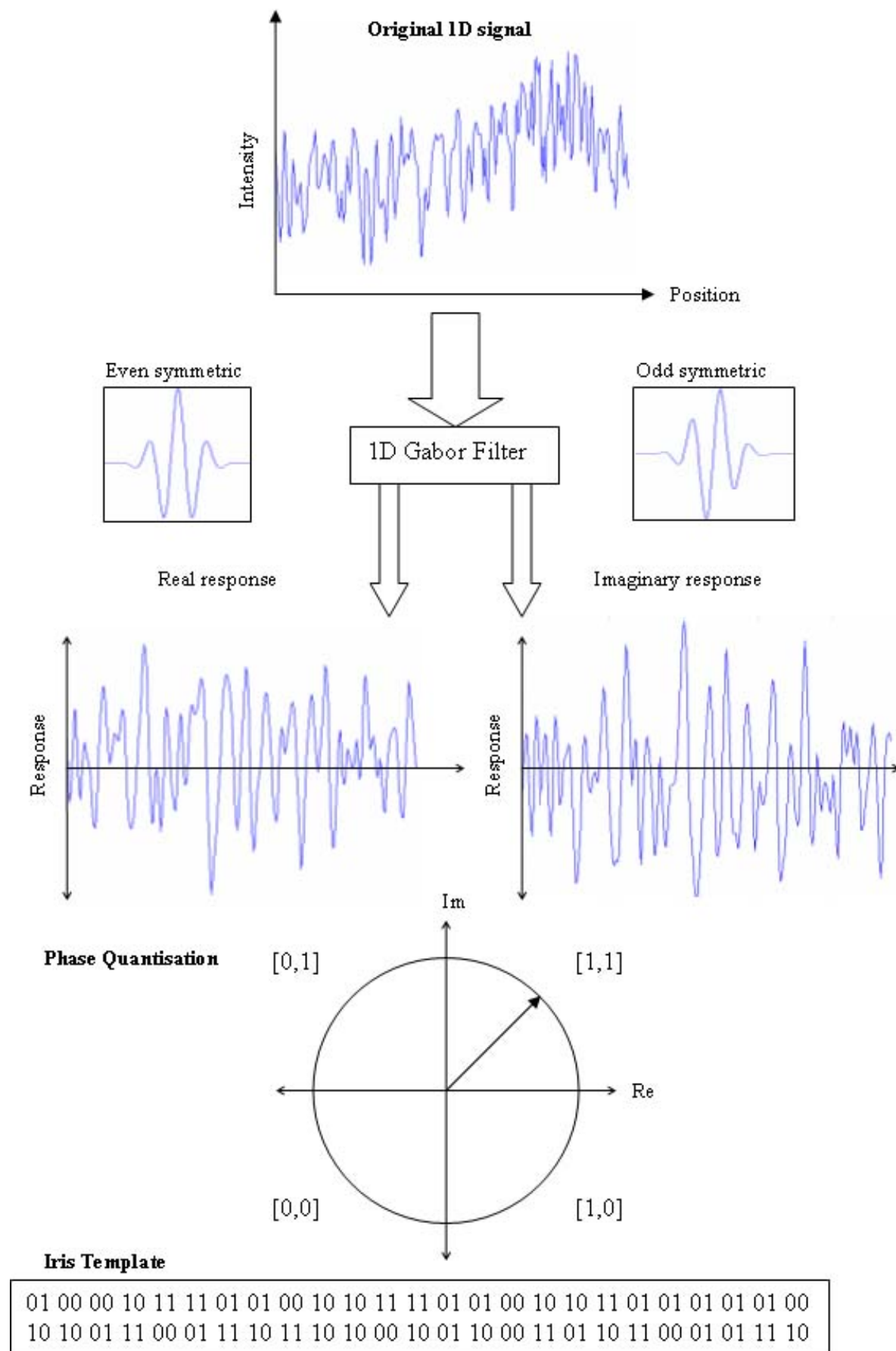
Figure 4.2 – An illustration of the feature encoding process.

4.4.2 Matching

For matching, the Hamming distance was chosen as a metric for recognition, since bit-wise comparisons were necessary. The Hamming distance algorithm employed also incorporates noise masking, so that only significant bits are used in calculating the Hamming distance between two iris templates. Now when taking the Hamming distance, only those bits in the iris pattern that correspond to '0' bits in noise masks of both iris patterns will be used in the calculation. The Hamming distance will be calculated using only the bits generated from the true iris region, and this modified Hamming distance formula is given as

$$HD = \frac{1}{N - \sum\limits_{k=1}^{N} Xn_k (OR) Yn_k} \sum\limits_{j=1}^{N} X_j (XOR) Y_j (AND) Xn'_j (AND) Yn'_j \qquad \textbf{(4.11)}$$

where Xj and Yj are the two bit-wise templates to compare, Xn_j and Yn_j are the corresponding noise masks for Xj and Yj, and N is the number of bits represented by each template.

Although, in theory, two iris templates generated from the same iris will have a Hamming distance of 0.0, in practice this will not occur. Normalisation is not perfect, and also there will be some noise that goes undetected, so some variation will be present when comparing two intra-class iris templates.

In order to account for rotational inconsistencies, when the Hamming distance of two templates is calculated, one template is shifted left and right bit-wise and a number of Hamming distance values are calculated from successive shifts. This bit-wise shifting in the horizontal direction corresponds to rotation of the original iris region by an angle given by the angular resolution used. If an angular resolution of 180 is used, each shift will correspond to a rotation of 2 degrees in the iris region. This method is suggested by Daugman [1], and corrects for misalignments in the normalised iris pattern caused by rotational differences during imaging. From the calculated Hamming distance values, only the lowest is taken, since this corresponds to the best match between two templates.

The number of bits moved during each shift is given by two times the number of filters used, since each filter will generate two bits of information from one pixel of the normalised region. The actual number of shifts required to normalise rotational inconsistencies will be determined by the maximum angle difference between two images of the same eye, and one shift is defined as one shift to the left, followed by one shift to the right. The shifting process for one shift is illustrated in Figure 4.3.
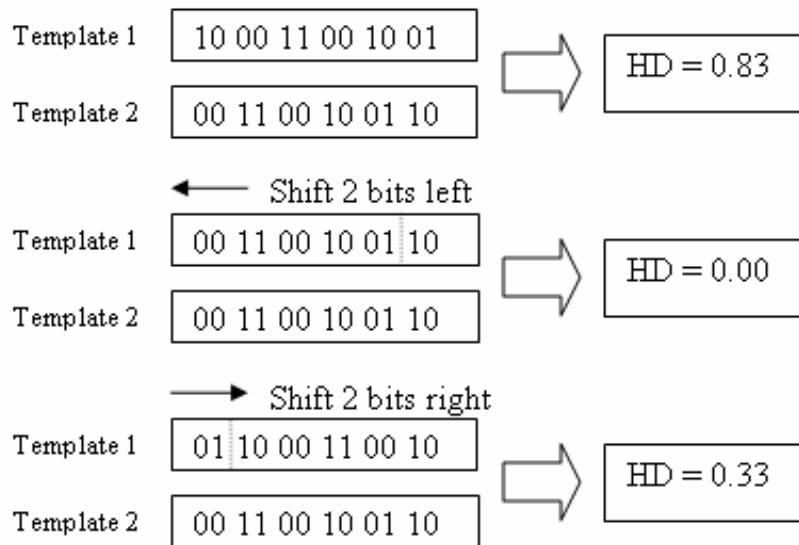
Figure 4.3 – An illustration of the shifting process. One shift is defined as one shift left, and one shift right of a reference template. In this example one filter is used to encode the templates, so only two bits are moved during a shift. The lowest Hamming distance, in this case zero, is then used since this corresponds to the best match between the two templates.

Chapter 5

Experimental Results

5.1 Overview

In this chapter, the performance of the iris recognition system as a whole is examined. Tests were carried out to find the best separation, so that the false match and false accept rate is minimised, and to confirm that iris recognition can perform accurately as a biometric for recognition of individuals. As well as confirming that the system provides accurate recognition, experiments were also conducted in order to confirm the uniqueness of human iris patterns by deducing the number of degrees of freedom present in the iris template representation.

There are a number of parameters in the iris recognition system, and optimum values for these parameters were required in order to provide the best recognition rate. These parameters include; the radial and angular resolution, r and θ respectively, which give the number of data points for encoding each template, and the filter parameters for feature encoding. The filter parameters include, the number of filters, N, their base wavelength λ_n, filter bandwidths given by σ/f, and the multiplicative factor between centre wavelengths of successive filters given by α. Also examined were the number of shifts required to account for rotational inconsistencies between any two iris representations.

5.2 Data Sets

5.2.1 Chinese Academy of Sciences - Institute of Automation

The Chinese Academy of Sciences - Institute of Automation (CASIA) eye image database [13] contains 756 greyscale eye images with 108 unique eyes or classes and 7 different images of each unique eye. Images from each class are taken from two sessions with one month interval between sessions. The images were captured especially for iris recognition research using specialised digital optics developed by the National Laboratory of Pattern Recognition, China. The eye images are mainly from persons of Asian decent, whose eyes are characterised by irises that are densely pigmented, and with dark eyelashes. Due to specialised imaging conditions using near infra-red light, features in the iris region are highly visible and there is good contrast between pupil, iris and sclera regions.

5.2.2 Lions Eye Institute

The Lions Eye Institute database [14] consists of 120 greyscale eye images taken using a slit lamp camera. Since the images were captured using natural light, specular reflections are present on the iris, pupil, and cornea regions. Unlike the CASIA database, the LEI database was not captured specifically for iris recognition.

5.2.3 Actual Data Sets

It was not possible to use all of the eye images from each database, since perfect segmentation success rates were not attained. Instead a sub-set of each database was selected, which contained only those images that were segmented successfully. The details of each sub-set are outlined in Table 5.1.

Set Name	Super Set	Number of Eye Images	Possible Intra-Class Comparisons	Possible Inter-Class Comparisons
CASIA-a	CASIA	624	1679	192,699
LEI-a	LEI	75	131	2646

Table 5.1 – Eye image sets used for testing the system.

With the 'CASIA-a' data set 192,699 unique inter-class comparisons are possible. In other words 192,699 Hamming distance values are calculated. However, with template shifting, the number of comparisons increases significantly. With 10 shifts left and right, that is 20 shifts in total, the 'CASIA-a' data set performs 3,853,980 unique comparisons when calculating all possible inter-class values, but only 192,699 Hamming distance values are used.

5.3   Uniqueness of Iris Patterns

5.3.1 Overview

The first test was to confirm the uniqueness of iris patterns. Testing the uniqueness of iris patterns is important, since recognition relies on iris patterns from different eyes being entirely independent, with failure of a test of statistical independence resulting in a match. Uniqueness was determined by comparing templates generated from different eyes to each other, and examining the distribution of Hamming distance values produced. This distribution is known as the inter-class distribution.

According to statistical theory, the mean Hamming distance for comparisons between inter-class iris templates will be 0.5. This is because, if truly independent, the bits in each template can be thought of as being randomly set, so there is a 50% chance of being set to 0 and a 50% chance of being set to 1. Therefore, half of the bits will agree between two templates, and half will disagree, resulting in a Hamming distance of 0.5.

The templates are shifted left and right to account for rotational inconsistencies in the eye image, and the lowest Hamming distance is taken as the actual Hamming distance. Due to this, the mean Hamming distance for inter-class template comparisons will be slightly lower than 0.5, since the lowest Hamming distance out of several comparisons between shifted templates is taken. As the number of shifts increases, the mean Hamming distance for inter-class comparisons will decrease accordingly.

Uniqueness was also be determined by measuring the number of degrees of freedom represented by the templates. This gives a measure of the complexity of iris patterns, and can be calculated by approximating the collection of inter-class Hamming distance values as a binomial distribution. The number of degrees of freedom, *DOF*, can be calculated by:

$$DOF = \frac{p(1-p)}{\sigma^2} \qquad \textbf{(5.1)}$$

where p is the mean, and σ is the standard deviation of the distribution.

5.3.2 Results
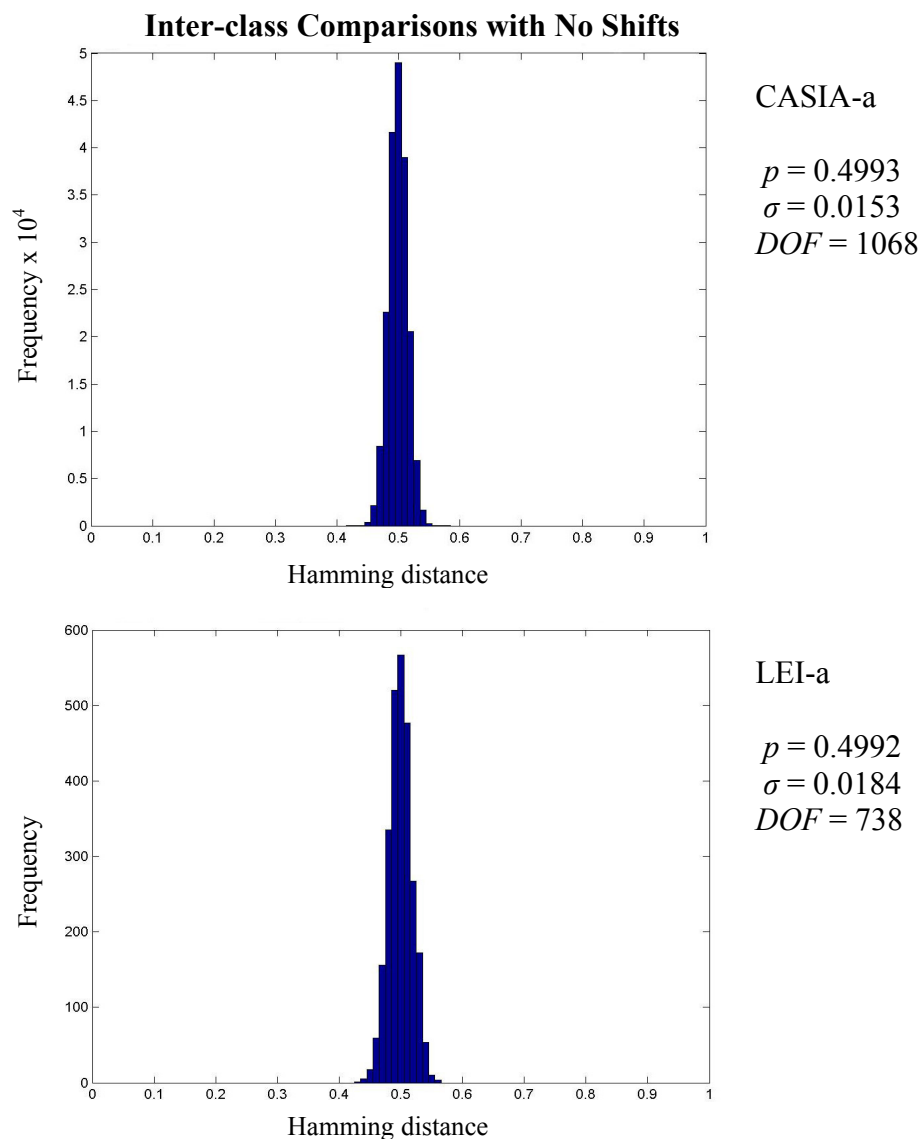
Figure 5.1 – Inter-class Hamming distance distribution of the 'CASIA-a' data set **(top)** and the 'LEI-a' data set **(bottom)** with no shifts when comparing templates. Encoded with one filter.

Inter-class Comparisons with 10 Shifts

CASIA-a

$p = 0.4757$
$\sigma = 0.0089$
$DOF = 3149$

LEI-a

$p = 0.4692$
$\sigma = 0.0121$
$DOF = 1701$
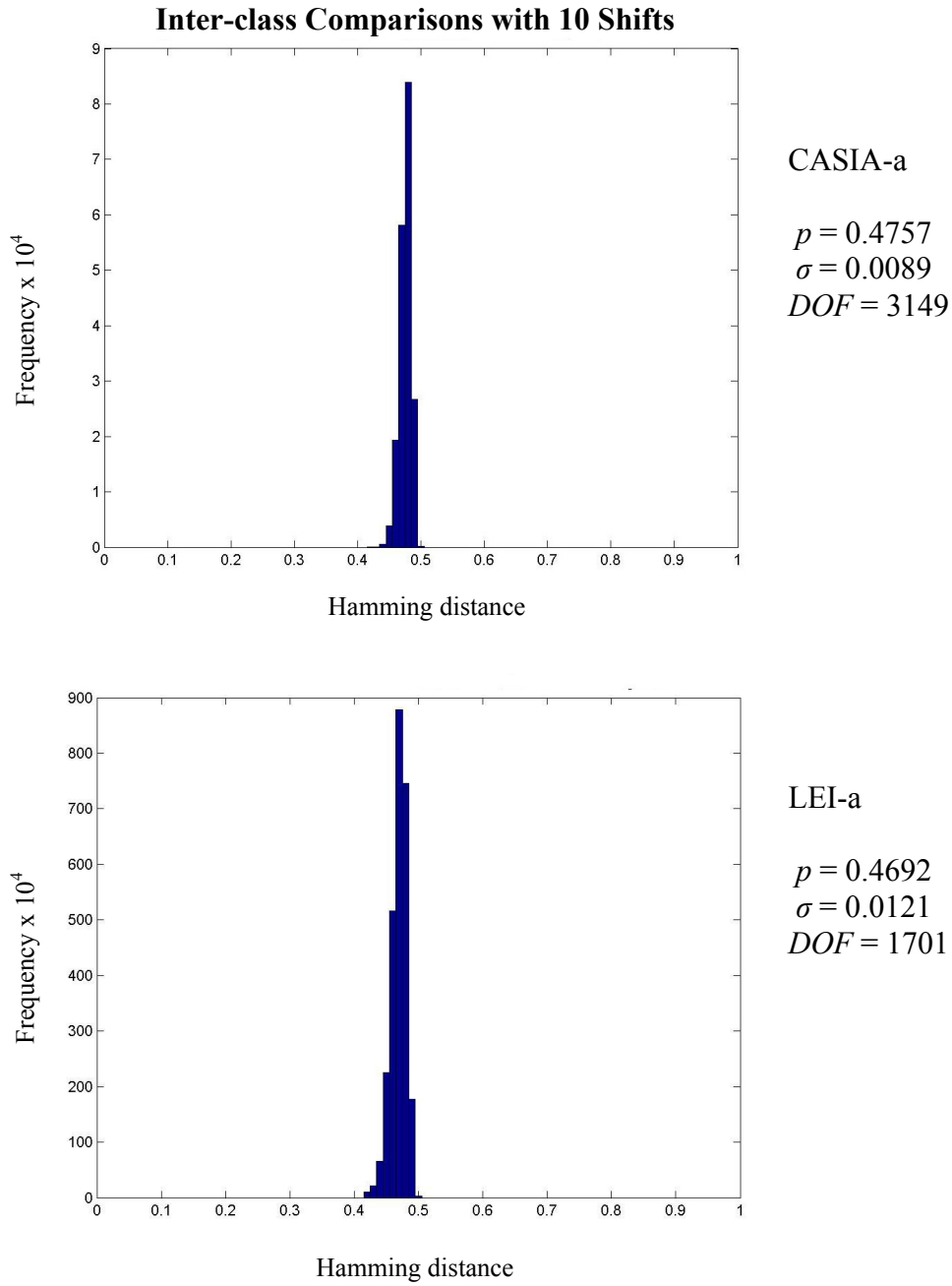
Figure 5.2 – Inter-class Hamming distance distribution of the 'CASIA-a' data set **(top)** and the 'LEI-a' data set **(bottom)** with 10 shifts left and right when comparing templates. Encoded with one filter.

5.3.3 Conclusion

As Figure 5.1 shows, the inter-class Hamming distance distributions conform to the theory of statistical independence, since the mean of the distribution equals 0.5. Therefore it can be stated that for both data sets, 'CASIA-a' and 'LEI-a', iris templates generated are highly unique, in that comparing any two templates generated from different irises is equivalent to comparing two random bit patterns. Also, the number of degrees calculated for both data sets shows the complexity of the iris, with

1068 degrees of freedom represented by the 'CASIA-a' data set, and 738 degrees of freedom represented by the 'LEI-a' data set.

As shifting was introduced, so that intra-class templates were properly lined up, the mean inter-class Hamming distance value decreased as expected. With 10 shifts the mean decreased to 0.47 for both 'CASIA-a' and 'LEI-a' data sets as shown in Figure 5.2. The standard deviation of inter-class distribution was also reduced, this was because the lowest value from a collection was selected, which reduced outliers and spurious values.

The shifting also caused a reduction in the number of degrees of freedom, *DOF*. This reduction in *DOF* is an anomaly caused by a smaller standard deviation, which itself is caused by taking the lowest Hamming distance from 10 calculated values. This shows that, due to shifting, the distribution is not merely shifted towards the left, but the characteristics of the distribution are changed. Therefore the degrees of freedom formula is not very useful with shifting introduced, since it relies on the distribution approximating a binomial.

5.4 Recognition of Individuals

5.4.1 Overview

The key objective of an iris recognition system is to be able to achieve a distinct separation of intra-class and inter-class Hamming distance distributions. With clear separation, a separation Hamming distance value can be chosen which allows a decision to be made when comparing two templates. If the Hamming distance between two templates is less than the separation point, the templates were generated from the same iris and a match is found. Otherwise if the Hamming distance is greater than the separation point the two templates are considered to have been generated from different irises.

The distance between the minimum Hamming distance value for inter-class comparisons and maximum Hamming distance value for intra-class comparisons could be used as a metric to measure separation; however, this is not a very accurate measure since outliers will corrupt the value calculated, and the measure is dependent on the number of iris templates compared. A better metric is 'decidability' [2], which takes into account the mean and standard deviation of the intra-class and inter-class distributions.

$$d' = \frac{\left|\mu_S - \mu_D\right|}{\sqrt{\frac{\left(\sigma_S^2 + \sigma_D^2\right)}{2}}} \qquad \textbf{(5.2)}$$

Decidability d' is a distance measured in standard deviations and is a function of the magnitude of difference between the mean of the intra-class distribution μ_s, and the mean of the inter-class distribution μ_s, and also the standard deviation of the intra-class and inter-class distributions, σ_S^2 and σ_D^2 respectively. The higher the

decidability, the greater the separation of intra-class and inter-class distributions, which allows for more accurate recognition.

With a pre-determined separation Hamming distance, a decision can be made as to whether two templates were created from the same iris (a match), or whether they were created from different irises. However, the intra-class and inter-class distributions may have some overlap, which would result in a number of incorrect matches or false accepts, and a number of mismatches or false rejects.

The false reject rate (FRR), also known as Type I error [25], measures the probability of an enrolled individual not being identified by the system. The false accept rate (FAR), also known as Type II error [25], measures the probability of an individual being wrongly identified as another individual. The false accept and false reject rates can be calculated by the amount of overlap between two distributions, which is illustrated in Figure 5.3. The false accept rate is defined by the normalised area between 0 and the separation point, κ, in the inter-class distribution P_{diff}. The false reject rate is defined as the normalised area between the separation point, κ, and 1 in the intra-class distribution P_{same}.

$$FAR = \frac{\int_0^\kappa P_{diff}(x)dx}{\int_0^1 P_{diff}(x)dx} \qquad (5.3)$$

$$FRR = \frac{\int_\kappa^1 P_{same}(x)dx}{\int_0^1 P_{same}(x)dx} \qquad (5.4)$$

Clearly the separation point will influence the false accept and false reject rates, since a lower separation Hamming distance will decrease *FAR* while increasing *FRR*, and vice versa. Therefore, when choosing a separation point it is important to consider both the false accept rate and false reject rate.

Intra-Class and Inter-Class Hamming Distance Distributions with Overlap
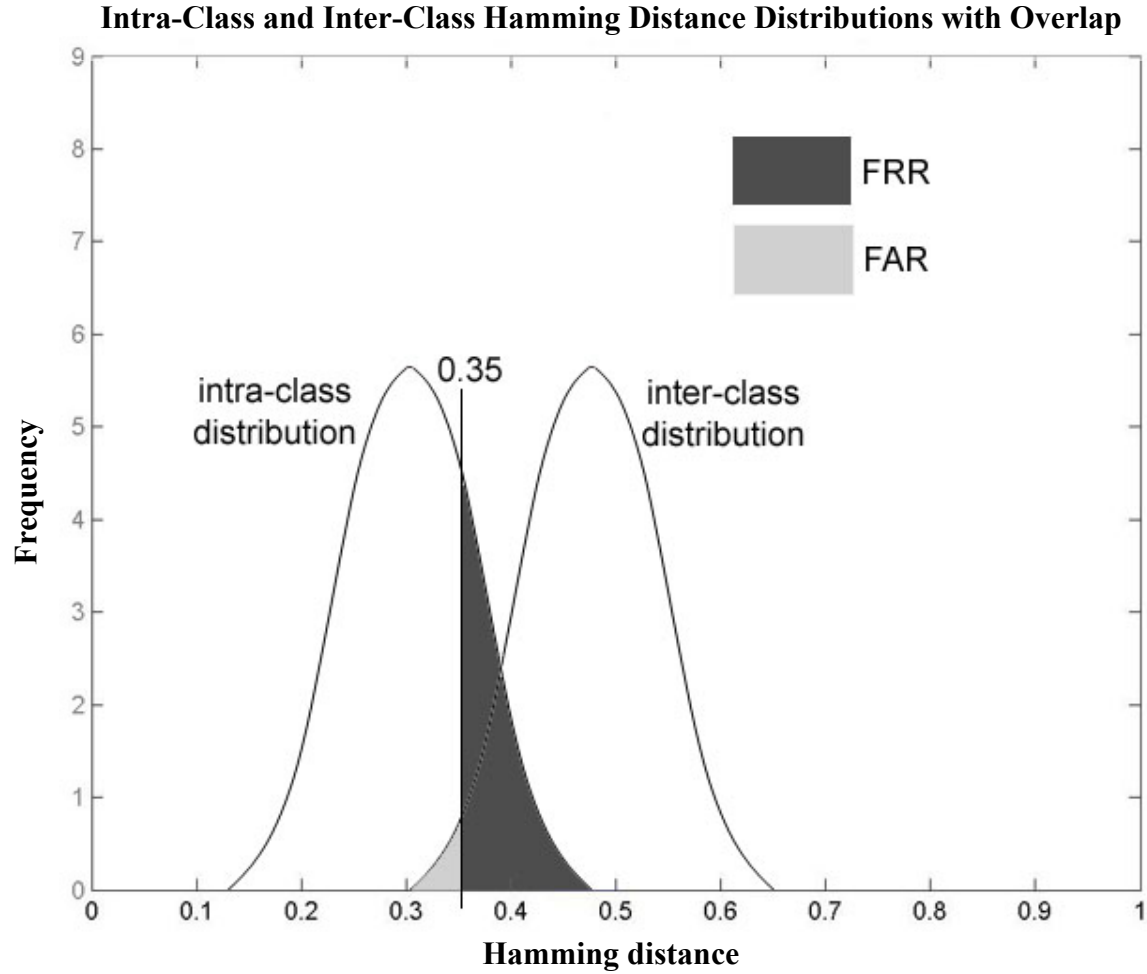
Figure 5.3 – False Accept and False Reject Rates for two distributions with a separation Hamming distance of 0.35.

The decidability metric will determine the optimum parameters. Once optimum parameters have been found, the performance of this optimal configuration will be measured by calculating the false accept and false reject rates.

5.4.2 Filter Parameters

For the encoding process the outputs of each filter should be independent, so that there are no correlations in the encoded template, otherwise the filters would be redundant. For maximum independence, the bandwidths of each filter must not overlap in the frequency domain, and also the centre frequencies must be spread out. Since information on filter parameters for encoding iris templates was lacking, the best filter parameters were found through experimentation with the 'LEI-a' data set. Once satisfactory filter parameters were found for the 'LEI-a' data set, they were tested on the 'CASIA-a' data set to compare performance. The 'CASIA-a' data set is relatively large and blind experimentation would have required continuously generating inter-class distributions until optimum parameters were found. Generation of the inter-class distribution is significantly more time consuming than with the 'LEI-a' data set, since millions rather than thousands of Hamming distance calculations are

required. The results of employing various filter parameters to encode iris templates are presented below.

Decidability vs Centre Wavelength for Three Different Filter Bandwidths
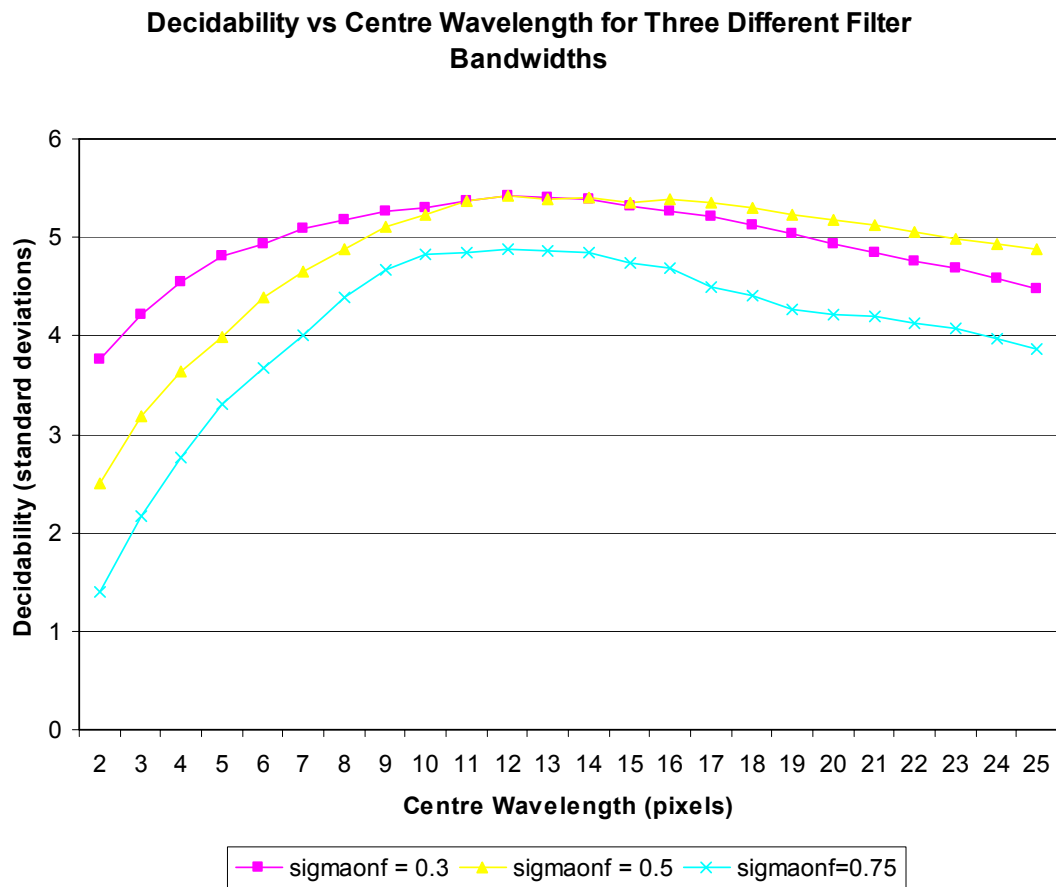
Figure 5.4 – Decidability of the 'LEI-a' data set encoded with a template size of 20x240, and with 3 shifts left and right. Values used in construction of this plot can be found in Appendix C.

N	λ_{min}	α	σ/f	μ_s	σ_s	μ_d	σ_d	d`
2	11.0	2.0	0.5	0.2421	0.0604	0.4808	0.0167	5.3848
2	11.0	3.0	0.5	0.2424	0.0610	0.4798	0.0218	5.1831
2	11.0	4.0	0.5	0.2469	0.0612	0.4786	0.0270	4.9024
2	11.0	5.0	0.5	0.2514	0.0629	0.4762	0.0320	4.5049
2	12.0	2.0	0.5	0.2396	0.0610	0.4801	0.0182	5.3410
2	12.0	3.0	0.5	0.2416	0.0614	0.4792	0.0238	5.1020
2	12.0	4.0	0.5	0.2464	0.0620	0.4775	0.0293	4.7651
2	12.0	5.0	0.5	0.2511	0.0643	0.4748	0.0343	4.3414
2	11.0	2.0	0.7	0.2477	0.0626	0.4806	0.0174	5.0720
2	11.0	3.0	0.7	0.2513	0.0639	0.4790	0.0238	4.7251
2	11.0	4.0	0.7	0.2561	0.0623	0.4793	0.0304	4.5500
2	11.0	5.0	0.7	0.2588	0.0650	0.4772	0.0357	4.1666
3	11.0	2.0	0.5	0.2416	0.0614	0.4789	0.0243	5.0827
3	11.0	3.0	0.5	0.2534	0.0661	0.4712	0.0389	4.0172
3	11.0	4.0	0.5	0.2608	0.0729	0.4702	0.0572	3.1967
3	11.0	5.0	0.5	0.2659	0.0782	0.4696	0.0679	2.7834

Table 5.2 – Decidability of the 'LEI-a' data set encoded using multiple filters with 3 shifts left and right, and a template size of 20x240.

Decidability vs Centre Wavelength for Sigma/f of 0.5
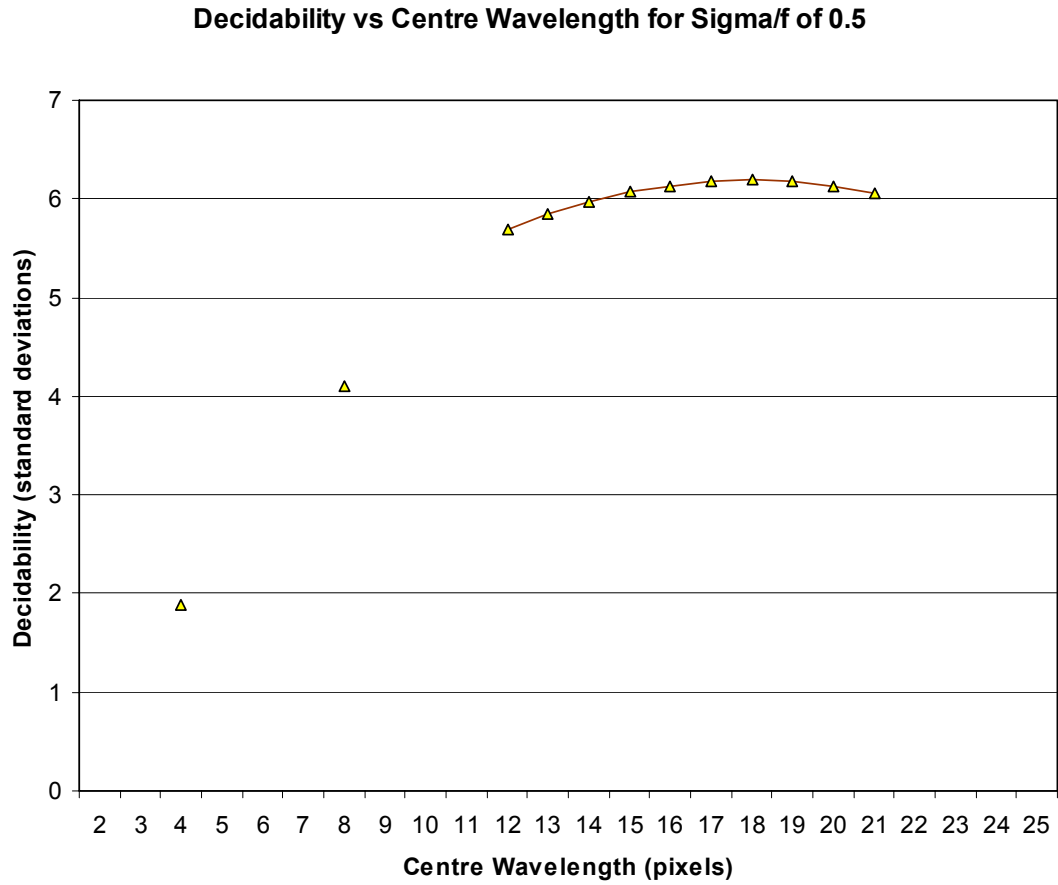
Figure 5.5 – Decidability verus centre wavelength for the CASIA-a data set using one filter, with bandwidth given by *σ/f* of 0.5. Values used in construction of this plot can be found in Appendix C.

N	λ_{min}	α	σ/f	μ_s	σ_s	μ_d	σ_d	d`
1	18.0	-	0.3	0.2881	0.0391	0.4553	0.0218	5.2807
2	18.0	2	0.5	0.2760	0.0414	0.4591	0.0224	5.5034
2	18.0	3	0.5	0.2691	0.0442	0.4444	0.0321	4.5367

Table 5.3 – Further testing of Filter parameters for 'CASIA-a' with template size of 20x240.

Figure   5.4   and

Decidability vs Centre Wavelength for Sigma/f of 0.5
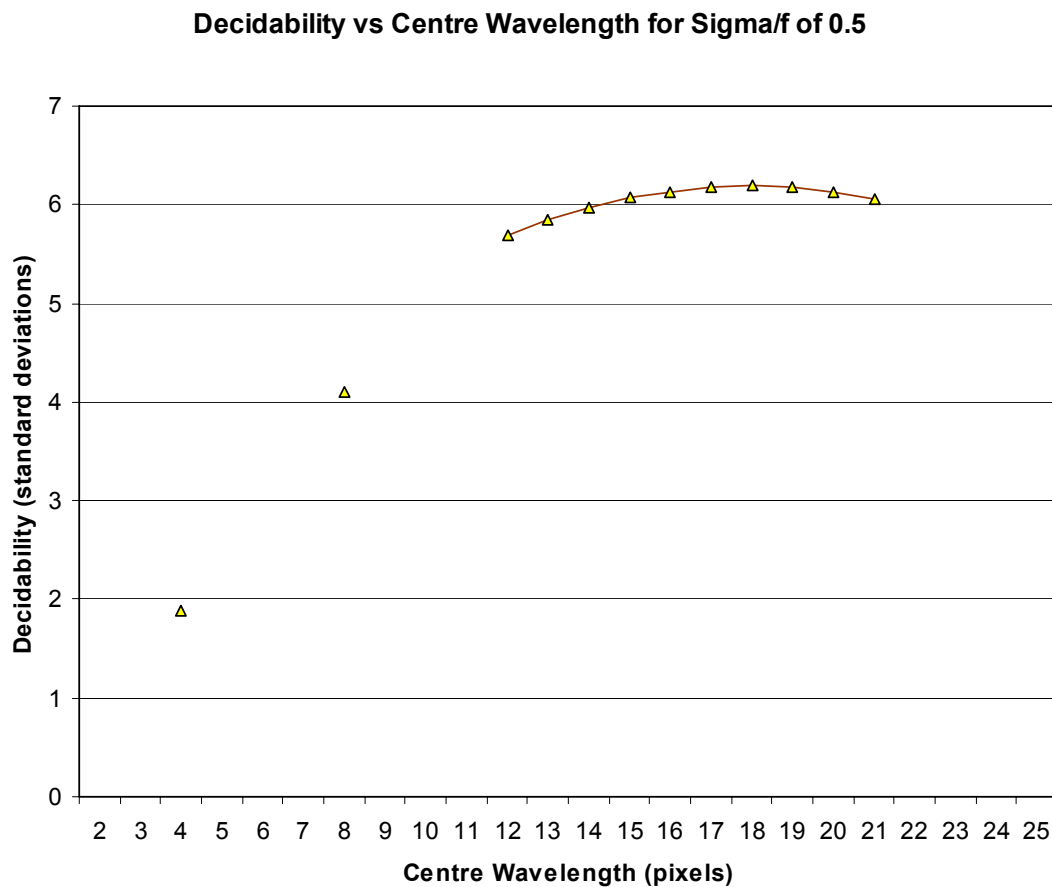
Figure **5.5** show that there exits an optimum centre wavelength for each data set, which produces maximum decidability. Furthermore, Table 5.2 and Table 5.3 show that encoding templates with multiple filters does not produce better decidability values, therefore the optimum number of filters is just one. As well as providing good representation of iris features, one filter also produces a compact iris template.

The optimum σ/f value was found to be 0.50, which corresponds to a filter bandwidth of around 2 octaves. However, the optimum centre wavelengths for the two data sets were found to be different. The 'LEI-a' was responsive to a centre wavelength of 12.0 pixels, which gave a maximum decidability of 5.4292. The 'CASIA-a' was sensitive to a centre wavelength of 18.0 pixels, which corresponded to a maximum decidability value of 6.1987. This difference in optimum wavelengths can be attributed to the different imaging conditions of each database, since it is stated by Daugman [2] that under infrared light, deeper and somewhat slowly modulated stromal features dominate the iris pattern. Also, the lower optimum decidability value for the 'LEI-a' data set can be attributed to undetected eyelashes within the iris region, which result in an increased standard deviation of the intra-class distribution and thus lower decidability value.

5.4.3 Template Resolution

One factor, which will significantly influence the recognition rate is the radial and angular resolution used during normalisation, since this determines the amount of iris

pattern data, which goes into encoding the iris template. Table 5.4 and Table 5.5 show decidability values generated from encoding templates with various radial and angular resolution dimensions.

	40	80	120	160	200	240	280
4	1.6814	3.2875	4.475	4.8079	5.101	5.1188	5.0576
8	1.8958	3.6256	4.6205	5.0381	5.2742	5.2933	5.0553
12	2.0018	3.7906	4.8951	5.3586	5.4307	5.4828	5.2459
16	2.0013	3.8192	4.7629	5.1884	5.3176	5.3291	5.1295
20	2.0261	3.8385	4.9318	5.3107	5.3854	5.4292	5.188
24	2.0436	3.7438	4.8384	5.2405	5.2859	5.3539	5.1141
28	2.0624	3.8248	4.8315	5.2278	5.3254	5.3568	5.1259
32	2.0878	3.8549	4.8623	5.2107	5.3158	5.3241	5.0838

Table 5.4 – Decidability of the 'LEI-a' data set with various template dimensions. Encoded using one filter with centre wavelength of 12.0 pixels, σ/*f* of 0.5, and performing 3 shifts left and right.

	40	80	120	160	200	240	280
4	1.2392	1.9836	3.0532	4.0734	4.7322	5.0275	5.4426
8	1.4138	2.3720	3.6138	4.8066	5.4537	5.5201	5.5323
12	1.4867	2.4373	3.8319	5.0286	5.6800	5.9310	5.9028
16	1.5139	2.5218	3.9394	5.1311	5.9114	6.1102	6.1344
20	1.5272	2.5400	3.9903	5.2281	6.0123	6.1987	6.2103
24	1.5270	2.5872	4.0103	5.3412	6.0939	6.2559	6.2748
28	1.5314	2.5805	4.1204	5.2810	6.1091	6.3134	6.2994
32	1.5412	2.5955	4.0903	5.3390	6.1832	6.3223	6.3111

Table 5.5 – Decidability of the 'CASIA-a' data set with various template dimensions. Encoded using one filter with centre wavelength of 18.0 pixels, σ/*f* of 0.5, and performing 8 shifts left and right.

The optimum template size for the 'LEI-a' data set was found to be 20x240, that is a radial resolution of 20 pixels, and an angular resolution of 240 pixels. For the 'CASIA-a' data set, the optimum template size was found to be 32x240 pixels. However, to provide a compact and efficient coding, a lower radial resolution can be used with only minor effect on decidability.

5.4.4 Number of shifts

The optimum number of template shifts to account for rotational inconsistencies can be determined by examining the mean and standard deviation of the intra-class distribution. Without template shifting the intra-class Hamming distance distribution will be more randomly distributed, since templates, which are not properly aligned, will produce Hamming distance values equivalent to comparing inter-class templates. As the number of shifts increases, the mean of the intra-class distribution will converge to a constant value, since all rotational inconsistencies would have been accounted for.
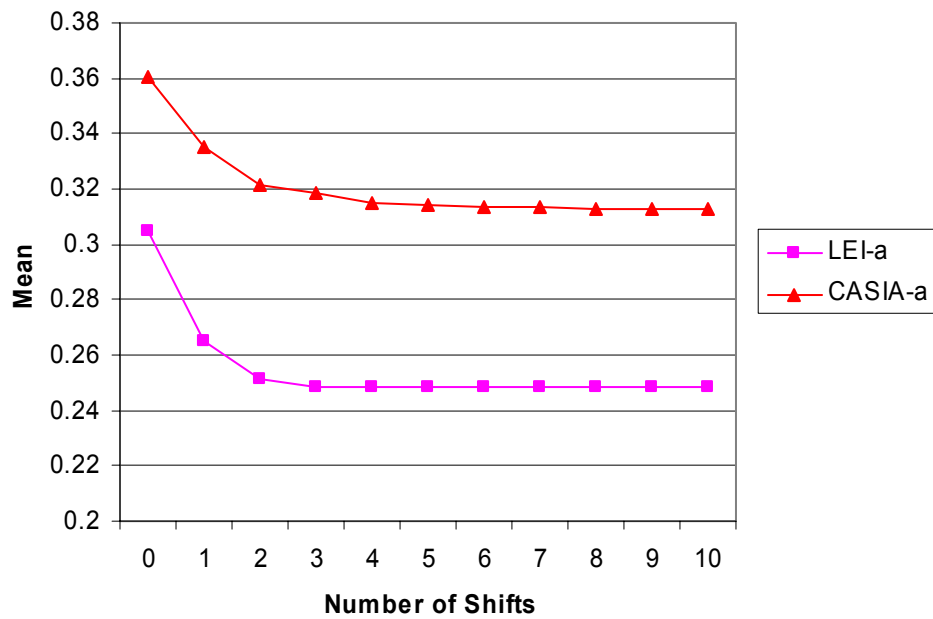
Figure 5.6 – Mean of the intra-class Hamming distance distribution as a function of the number of shifts performed. Values used in construction of this plot can be found in Appendix C.
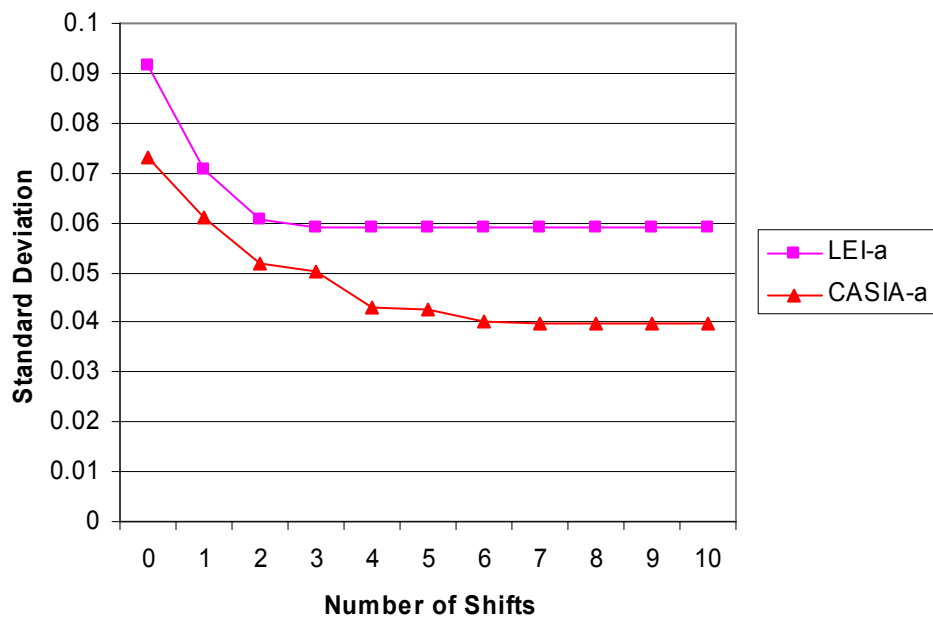
Figure 5.7 – Standard deviation of the intra-class Hamming distance distribution as a function of the number of shifts performed. Values used in construction of this plot can be found in Appendix C.

Intra-Class Distribution with 0 Shifts

$\mu_s = 0.3602$
$\sigma_s = 0.0731$
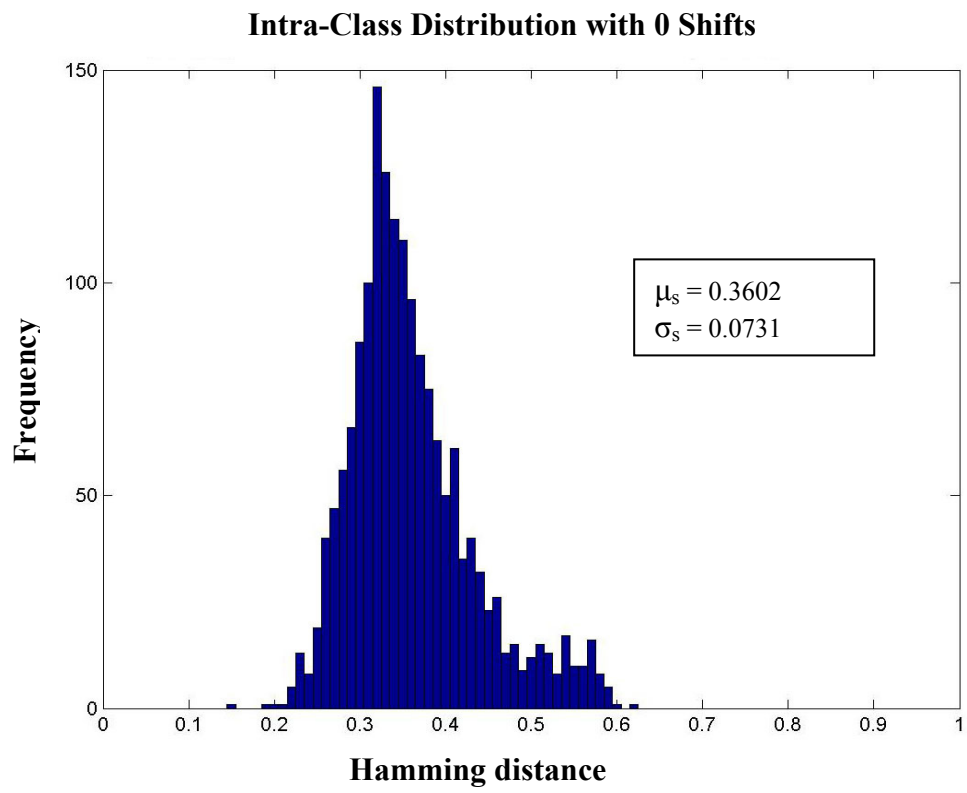
Figure 5.8 – Intra-class distribution of the 'CASIA-a' data set with no shifts.

Intra-Class Distribution with 4 Shifts Left and Right

$\mu_s = 0.3150$
$\sigma_s = 0.0431$
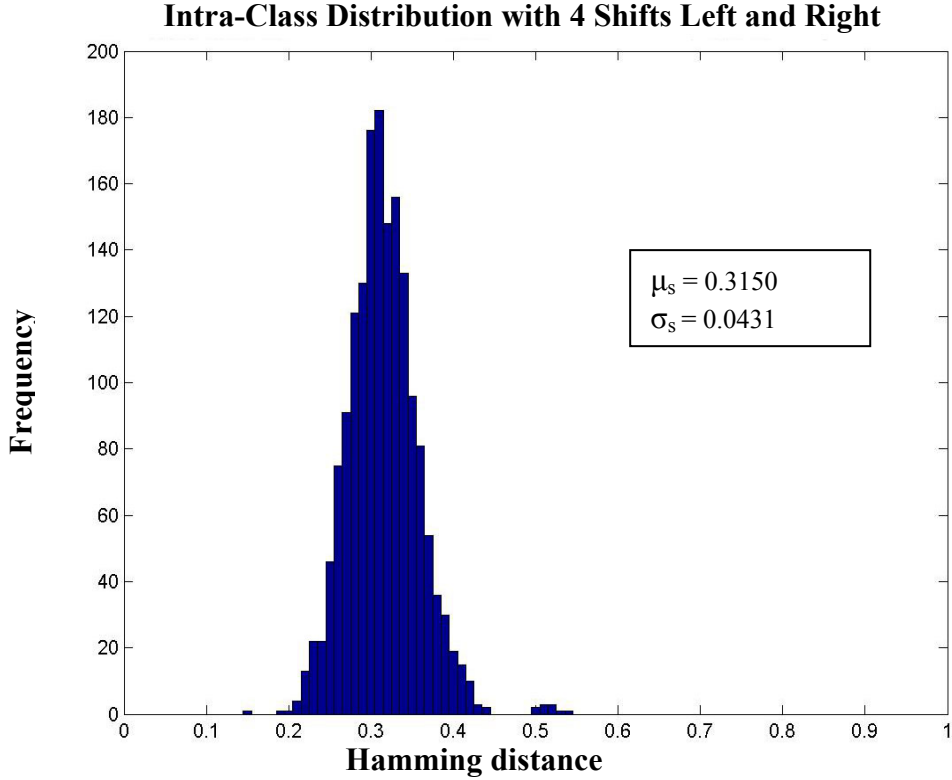
Figure 5.9 - Intra-class distribution of the 'CASIA-a' data set with 4 shifts left and right.

With reference to Figure 5.6 and Figure 5.7, the 'LEI-a' data set reaches its minimum mean and standard deviation after 3 shifts, while the 'CASIA-a' data set requires 8 shifts to reach its minimum. However, it is noted that 4 shifts are enough to be able to account for most of the rotational inconsistencies in the 'CASIA-a' data set.

It can be seen from Figure 5.8 that with zero shifts of templates, the intra-class Hamming distance values become spread out towards 0.5, since due to rotational inconsistencies a significant number of templates are not aligned. Also, there are a number of Hamming distance values around 0.6. This shows that when templates are misaligned their bit patterns become almost inverted, resulting in a high ratio of disagreeing bits. With 10 shifts left and right the intra-class Hamming distance values become much closer distributed around the mean, since rotational inconsistencies have now been eliminated.

5.4.5 Conclusion

In summary, the optimum encoding of iris features was with one 1D Log-Gabor filter with a bandwidth given by a σ/f of 0.5. The centre wavelength of this filter was found to be dependent on the data set used. A centre wavelength of 12.0 pixels provided optimum decidability for the 'LEI-a', while 18.0 pixels proved optimal for the 'CASIA-a' data set. An optimum template size with radial resolution of 20 pixels, and angular resolution of 240 pixels was chosen for both data sets. These parameters generate a biometric template that contains 9600 bits of information. In order to correct for rotational inconsistencies 3 shifts left and right were required for each comparison of templates from the 'LEI-a' data set, and 8 shifts left and right were

required when comparing templates from the 'CASIA-a' data set. Now that optimum parameters have been determined, the recognition performance was examined next.

Intra-class and Inter-class Distributions
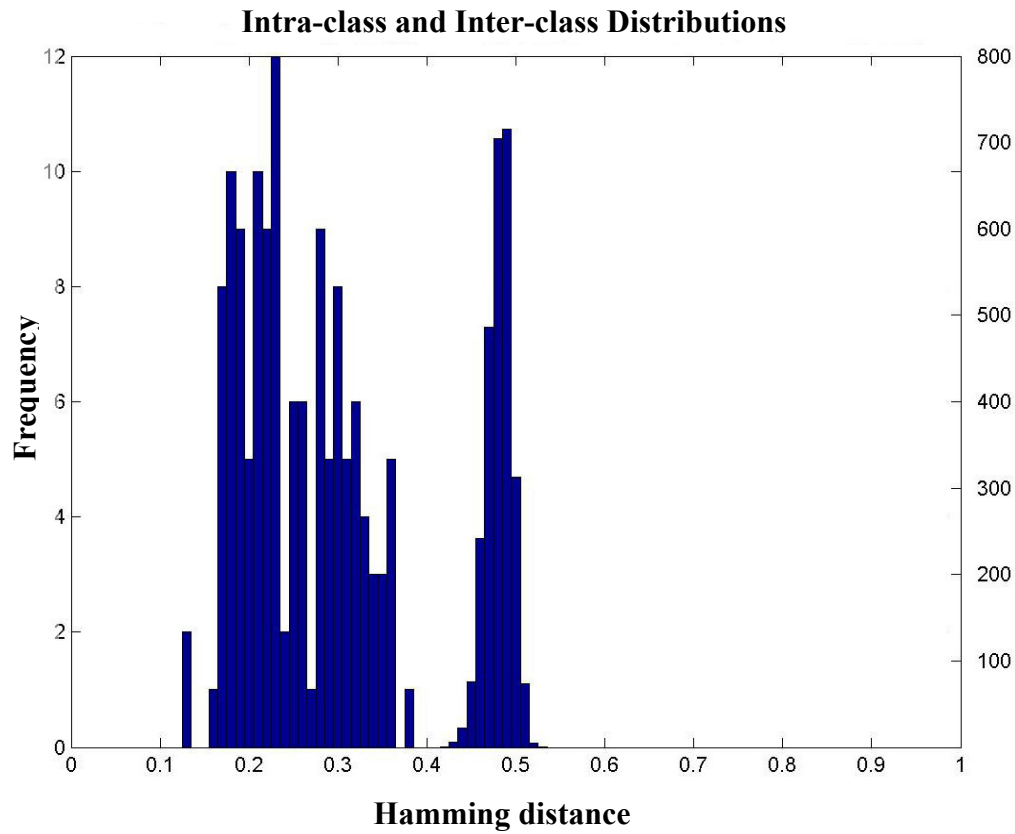
Figure 5.10 – Distribution of intra-class and inter-class Hamming distances using the 'LEI-a' data set, encoded with one filter with centre wavelength of 12.0 pixels, σ/f of 0.5, template size of 20x240, and 3 shifts left and right.

The above figure shows a good separation of intra-class and inter-class Hamming distance values. A Hamming distance value of 0.4 can be chosen as a separation point, so that if any two templates generate a Hamming distance value greater than 0.4, they are deemed to be generated from different irises. If two templates generate a Hamming distance value lower than 0.4 then the two are deemed to be from the same iris.
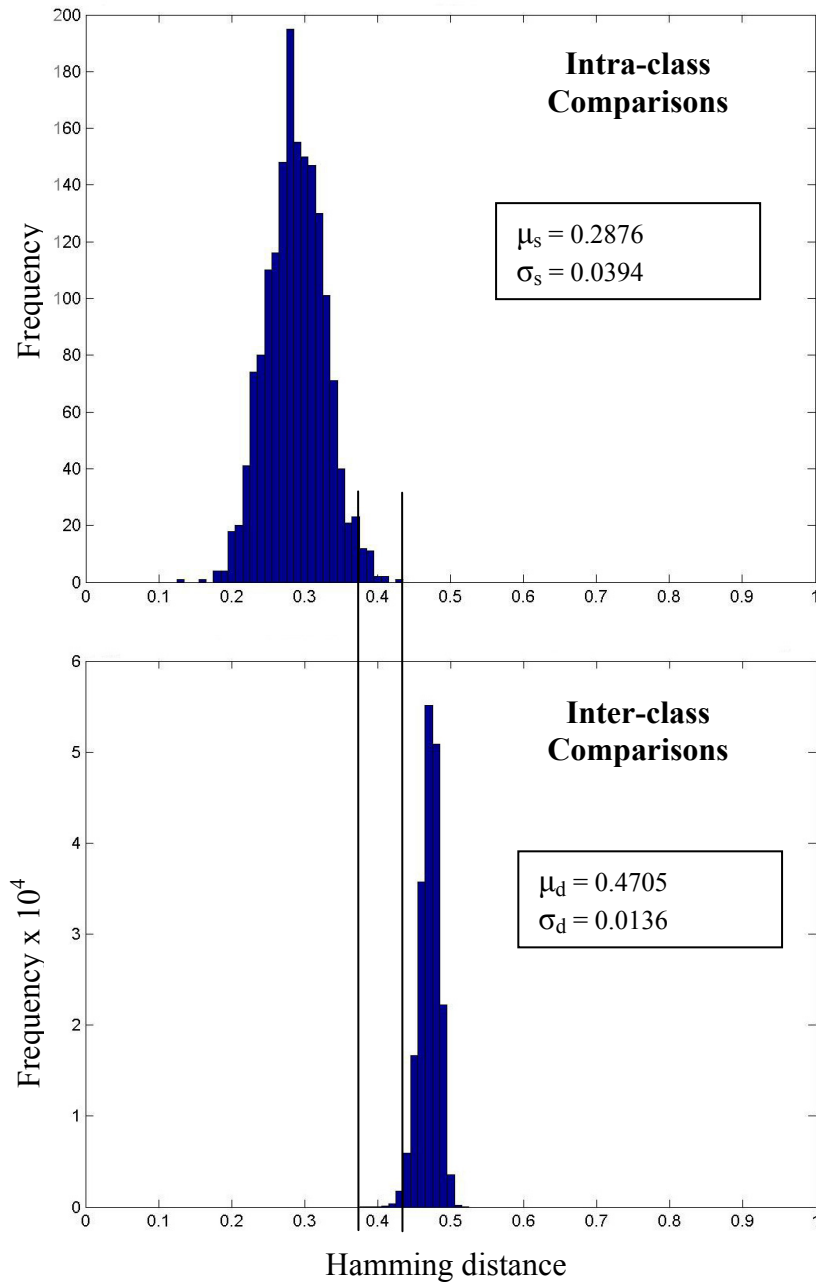
Figure 5.11 – Distribution of intra-class and inter-class Hamming distances using the 'CASIA-a' data set, encoded with one filter with centre wavelength of 18.0 pixels, σ/f of 0.5, template size of 20x240, and 8 shifts left and right.

Figure 5.10 and Figure 5.11 show Hamming distance distributions with slight overlap. However, the means of the intra-class and inter-class distributions are still clearly separated, so recognition is still possible. The accuracy of recognition with these distributions can be determined by calculating their false accept and false reject rates with different separation points.

Threshold	FAR (%)	FRR (%)
0.20	0.000	74.046
0.25	0.000	45.802
0.30	0.000	25.191
0.35	0.000	4.580
0.40	0.000	0.000
0.45	2.494	0.000
0.50	92.819	0.000

Table 5.6 – False accept and false reject rates for the 'LEI-a' data set with different separation points using the optimum parameters.

Threshold	FAR (%)	FRR (%)
0.20	0.000	99.047
0.25	0.000	82.787
0.30	0.000	37.880
0.35	0.000	5.181
0.40	0.005	0.238
0.45	7.599	0.000
0.50	99.499	0.000

Table 5.7 – False accept and false reject rates for the 'CASIA-a' data set with different separation points using the optimum parameters.

For the 'LEI-a' data set, perfect recognition is possible by selecting a separation Hamming distance of 0.40, which gives false accept rate and false reject rate both as 0.000%. However, with the 'CASIA-a' data set perfect recognition is not possible due to the overlapping distributions. With a separation point of 0.4 a false accept rate and false reject rate of 0.005% and 0.238% respectively is achieved, which still allows for accurate recognition.

Chapter 6

Conclusion

6.1 Summary of Work

This thesis has presented an iris recognition system, which was tested using two databases of greyscale eye images in order to verify the claimed performance of iris recognition technology.

Firstly, an automatic segmentation algorithm was presented, which would localise the iris region from an eye image and isolate eyelid, eyelash and reflection areas. Automatic segmentation was achieved through the use of the circular Hough transform for localising the iris and pupil regions, and the linear Hough transform for localising occluding eyelids. Thresholding was also employed for isolating eyelashes and reflections.

Next, the segmented iris region was normalised to eliminate dimensional inconsistencies between iris regions. This was achieved by implementing a version of Daugman's rubber sheet model, where the iris is modelled as a flexible rubber sheet, which is unwrapped into a rectangular block with constant polar dimensions.

Finally, features of the iris were encoded by convolving the normalised iris region with 1D Log-Gabor filters and phase quantising the output in order to produce a bit-wise biometric template. The Hamming distance was chosen as a matching metric, which gave a measure of how many bits disagreed between two templates. A failure of statistical independence between two templates would result in a match, that is, the two templates were deemed to have been generated from the same iris if the Hamming distance produced was lower than a set Hamming distance.

6.2 Summary of Findings

Analysis of the developed iris recognition system has revealed a number of interesting conclusions. It can be stated that segmentation is the critical stage of iris recognition, since areas that are wrongly identified as iris regions will corrupt biometric templates resulting in very poor recognition. The results presented in Chapter 2 have also shown that segmentation can be the most difficult stage of iris recognition because its success is dependent on the imaging quality of eye images. With the LEI database only 62% of the images managed to segment successfully due to poor imaging conditions, while 83% of the CASIA database images segmented correctly.

Another interesting finding was that the encoding process only required one 1D Log-Gabor filter to provide accurate recognition, since the open literature mentions the use of multi-scale representation in the encoding process. Also the optimum centre

wavelength was found to be dependent on imaging conditions, since different lighting conditions will produce features of different frequencies.

The optimum centre wavelength for the 'LEI-a' data set was found to be 12.0 pixels, while the 'CASIA-a' provided optimum recognition when encoded using a filter with centre wavelength of 18.0 pixels. For both data sets, a filter bandwidth with σ/f of 0.5, and template resolution of 20 pixels by 240 pixels was found to provide optimum encoding. For the 'LEI-a' data set, perfect recognition was possible with false accept and false reject rates of 0%. A near-perfect recognition rate was achieved with the 'CASIA-a' data set, with a separation point of 0.4, a false accept rate of 0.005% and false reject rate of 0.238% was possible. These results confirm that iris recognition is a reliable and accurate biometric technology.

6.3   Suggestions for Future Work

The system presented in this publication was able to perform accurately, however there are still a number of issues which need to be addressed. First of all, the automatic segmentation was not perfect, since it could not successfully segment the iris regions for all of the eye images in the two databases. In order to improve the automatic segmentation algorithm, a more elaborate eyelid and eyelash detection system could be implemented, such as the one suggested by Kong and Zhang [15].

An improvement could also be made in the speed of the system. The most computation intensive stages include performing the Hough transform, and calculating Hamming distance values between templates to search for a match. Since the system is implemented in MATLAB®, which is an interpreted language, speed benefits could be made by implementing computationally intensive parts in C or C++. Speed was not one of the objectives for developing this system, but this would have to be considered if using the system for real-time recognition.

Another extension to the system would be to interface it to an iris acquisition camera. Now rather than having a fixed set of iris images from a database, a frame grabber can be used to capture a number of images, possibility improving the recognition rate.

An optimisation whose feasibility could be examined with use of an acquisition camera would be the use of both eyes to improve the recognition rate. In this case, two templates would be created for each individual, one for the left eye and one for the right eye. This configuration would only accept an individual if both eyes match to corresponding templates stored in the database. The recognition rates produced for this optimisation would need to be balanced with the increased imaging difficultly, and inconvenience to the user.

6.4   Anomalies

Although the developed system has recorded good results with the data sets presented, there are still some factors to consider if the software was to be used with a hardware camera. Contact lenses are available which can change the colour of an individual's iris. These present a problem to any iris recognition system, since a fake iris pattern is

printed on the surface of the lens, and will falsely reject an enrolled user, or falsely accept them, if the fake iris pattern has been enrolled in the database.

Another problem to consider, although it would be quite minor, is that the border of any contact lens is slightly visible in an eye image, and this circular border may confuse the automatic segmentation algorithm in detecting it as the iris boundary. Also, a high portion of the population wear spectacles, so if imaging the eye region, the spectacles may introduce too much specular reflection resulting in failure of automatic segmentation and/or recognition.

A high-resolution photograph of a human eye could also be presented to an iris recognition camera, resulting in an unauthorised match. Wildes presents a solution to counteract this by using the fact that a live iris will undergo a constant state of small oscillation [4]. Wildes suggests that this situation can be avoided by checking for these small changes in pupil size between successive captures of the eye. Although, these factors are rarely considered in the open literature, they are critical to the accuracy and success of iris recognition as a biometric technology.

The MATLAB® source code for the iris recognition software presented in this publication is available via the World Wide Web at the address.
http://www.csse.uwa.edu.au/~masekl01/

Bibliography

[1]   S. Sanderson, J. Erbetta. Authentication for secure environments based on iris scanning technology. *IEE Colloquium on Visual Biometrics*, 2000.

[2]   J. Daugman. How iris recognition works. Proceedings of 2002 International Conference on Image Processing, Vol. 1, 2002.

[3]   E. Wolff. *Anatomy of the Eye and Orbit*. 7th edition. H. K. Lewis & Co. LTD, 1976.

[4]   R. Wildes. Iris recognition: an emerging biometric technology. *Proceedings of the IEEE*, Vol. 85, No. 9, 1997.

[5]   J. Daugman. Biometric personal identification system based on iris analysis. United States Patent, Patent Number: 5,291,560, 1994.

[6]   J. Daugman. High confidence visual recognition of persons by a test of statistical independence. *IEEE Transactions on Pattern Analysis and Machine Intelligence*, Vol. 15, No. 11, 1993.

[7]   R. Wildes, J. Asmuth, G. Green, S. Hsu, R. Kolczynski, J. Matey, S. McBride. A system for automated iris recognition. *Proceedings IEEE Workshop on Applications of Computer Vision*, Sarasota, FL, pp. 121-128, 1994.

[8]   W. Boles, B. Boashash. A human identification technique using images of the iris and wavelet transform. *IEEE Transactions on Signal Processing*, Vol. 46, No. 4, 1998.

[9]   S. Lim, K. Lee, O. Byeon, T. Kim. Efficient iris recognition through improvement of feature vector and classifier. *ETRI Journal*, Vol. 23, No. 2, Korea, 2001.

[10]   S. Noh, K. Pae, C. Lee, J. Kim. Multiresolution independent component analysis for iris identification. *The 2002 International Technical Conference on Circuits/Systems, Computers and Communications*, Phuket, Thailand, 2002.

[11]   Y. Zhu, T. Tan, Y. Wang. Biometric personal identification based on iris patterns. *Proceedings of the 15th International Conference on Pattern Recognition*, Spain, Vol. 2, 2000.

[12]   C. Tisse, L. Martin, L. Torres, M. Robert. Person identification technique using human iris recognition. *International Conference on Vision Interface*, Canada, 2002.

[13]   Chinese Academy of Sciences – Institute of Automation. *Database of 756 Greyscale Eye Images*. http://www.sinobiometrics.com Version 1.0, 2003.

[14]   C. Barry, N. Ritter. *Database of 120 Greyscale Eye Images*. Lions Eye Institute, Perth Western Australia.

[15]   W. Kong, D. Zhang. Accurate iris segmentation based on novel reflection and eyelash detection model. *Proceedings of 2001 International Symposium on Intelligent Multimedia, Video and Speech Processing*, Hong Kong, 2001.

[16]   L. Ma, Y. Wang, T. Tan. Iris recognition using circular symmetric filters. National Laboratory of Pattern Recognition, Institute of Automation, Chinese Academy of Sciences, 2002.

[17]   N. Ritter. Location of the pupil-iris border in slit-lamp images of the cornea. *Proceedings of the International Conference on Image Analysis and Processing*, 1999.

[18]   M. Kass, A. Witkin, D. Terzopoulos. Snakes: Active Contour Models. *International Journal of Computer Vision*, 1987.

[19]   N. Tun. *Recognising Iris Patterns for Person (or Individual) Identification*. Honours thesis. The University of Western Australia. 2002.

[20]   D. Field. Relations between the statistics of natural images and the response properties of cortical cells. *Journal of the Optical Society of America*, 1987.

[21]   P. Burt, E. Adelson. The laplacian pyramid as a compact image code. *IEEE Transactions on Communications*. Vol. 31 No. 4. 1983.

[22]   P. Kovesi. *MATLAB Functions for Computer Vision and Image Analysis*.Available at: http://www.cs.uwa.edu.au/~pk/Research/MatlabFns/index.html

[23]   A. Oppenheim, J. Lim. The importance of phase in signals. *Proceedings of the IEEE 69*, 529-541, 1981.

[24]   P. Burt, E. Adelson. The laplacian pyramid as a compact image code. *IEE Transactions on Communications*, Vol. COM-31, No. 4, 1983.

[25]   J. Daugman. Biometric decision landscapes. *Technical Report No. TR482, University of Cambridge Computer Laboratory,* 2000.

[26]   T. Lee. Image representation using 2D gabor wavelets. *IEEE Transactions of Pattern Analysis and Machine Intelligence*, Vol. 18, No. 10, 1996.

Appendix A

Original Honours Proposal

Updated 12 June 2003

Title: Human Iris Patterns as a Form of Biometric Identification
Author: Libor Masek (masekl01@csse.uwa.edu.au)
Supervisor: Dr. Peter Kovesi

Background

The human iris contains a very unique pattern which can be used as the basis for biometric identification of individuals. Iris patterns possess high inter-class dependency, and low intra-class dependency [6], furthermore, the iris is enclosed by the cornea, making the iris pattern stable throughout adult life. These features make iris recognition, potentially, a very accurate biometric technology, allowing non-intrusive scanning with a low failure rate.

Iris recognition involves first extracting the iris from a digital eye image, and then encoding the unique patterns of the iris in such a way that they can be compared with pre-registered iris patterns. Since each individual iris has enormous pattern variability [6], large databases can be searched without fear of a false match.

The most widely used and successful commercial iris recognition system was developed and patented by Daugman [5] in 1994. Trials of Daugman's system have reported a false error match rate of zero [6], a very impressive figure when compared with systems such as facial recognition with error rates of around 50% [6]. Many other systems have been developed or proposed which use similar techniques to Daugman. These include prototype systems developed by Wildes et al [4], and Boles [8].

Aim

The goal of my project will be to develop an open source implementation of Daugman's system, in order to independently evaluate the algorithm. More specific goals of my project will be to automate the segmentation of the iris, previously done manually by Tun [19], and investigation of optimum parameters for biometric template encoding.

Although the techniques of Daugman will be studied closely, I will also experiment with other techniques, such as those documented by Wildes et al. [4], Boles [8] and

Kong et al. [15]. I will develop a generic open-source implementation rather than one based entirely on Daugman's methods.

Method

The first stage will be to develop an algorithm to automatically segment the iris region from an eye image. This will require research into many different techniques such as Daugman's integro-differential operator, circular Hough transform, and active contour models [18].

Following this, the next stage will be to normalize the iris region in order to counteract imaging inconsistencies such as pupil dilation. An implementation of Daugman's polar representation [2] will be used for this purpose, as this is the most documented method for iris normalization.

Once a normalised iris pattern has been obtained, it will be convolved with 2D Gabor wavelets in order to extract features. This method is well documented in papers by Daugman [2], and also Boles [8] and a MATLAB$^{®}$ function by Kovesi [22] is available to perform Gabor wavelet analysis.

Finally, matching and statistical analysis will be performed in order to test how well iris patterns can be identified against a database of pre-registered iris patterns. Again, this is well documented in the open literature.

In the early stages of the project, the primary objective will be to get results. Once results are obtained and analysed, the different parts of the software will be optimised, corrected and matching re-run. This iterative cycle will proceed until satisfactory results are obtained.

Wk	Uni.	Project Activities	Deadlines
10	1	Study segmentation techniques	
11	2		
12	3	Implement segmentation	Proposal due
13	4	Implement normalisation	
14	5	Study wavelets	
15	6	Implement feature encoding	
16	7		
17	Break	Study matching, start literature review	
18	8	Implement matching and comparison testing	
19	9		
20	10		
21	11	Run matching, Study and analyse results of matching	
22	12		
23	13		
24	Break	Exam preparation	Updated Proposal due
25	Exams		
26			
27	Break	Continue work on matching	
28			
29		Start dissertation	
30	1	Experiment with segmentation, and perfect and	
31	2	optimize segmentation	

32	3		
33	4	Perfect feature encoding, perform matching and study	
34	5	results. Experiment with parameters and tweak code	
35	6		
36	7		
37	8	Write up draft dissertation for review	
38	9		
39	Break		Draft dissertation due
40		Dissertation	
41	10		
42	11		
43	12	Seminar preparation, and finalising of dissertation	Project seminar
44	13		
45	Break		Final dissertation due

Table A.1 – Project Timetable

Software and Hardware Requirements

The software to perform iris recognition will be developed using the MATLAB[®] development environment. Coding will be done using a modular approach, so that key components can be updated and tested independently.

A computer system with an Intel Pentium IV processor running at 2533 MHz will be used; this should provide adequate processing power for compute intensive parts of the software, such as segmentation, and matching.

In order to further improve performance, compute intensive parts of the software can be written in C, using MATLAB[®] MEX files. However, this will be a low priority activity and will only be done if time permits.

Appendix B

System Overview
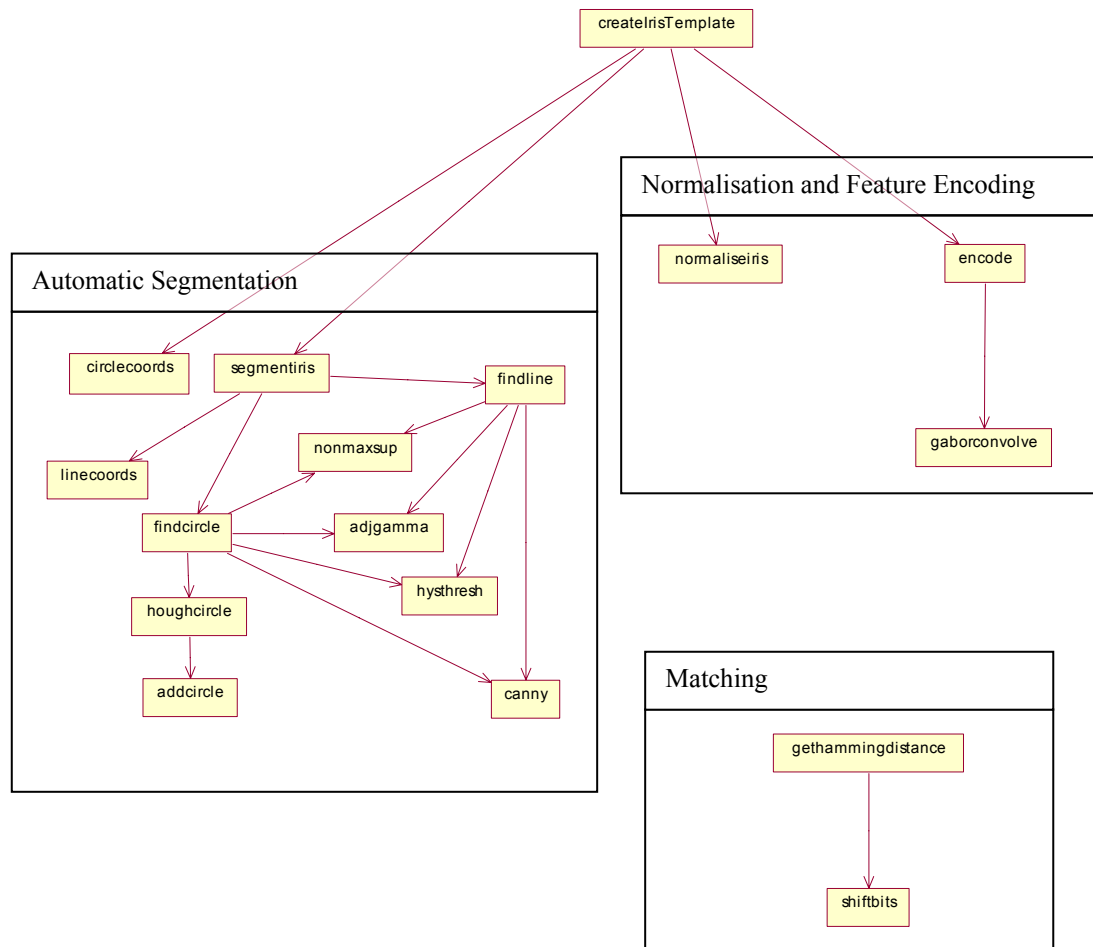
Figure B.1 – An overview of the sub-systems and MATLAB® functions that make up the iris recognition software system.

Appendix C

Detailed Experimental Results

λ_{min}	μ_s	σ_s	μ_d	σ_d	d`	DOF
2.0	0.4522	0.0317	0.4843	0.0073	1.3910	4640
3.0	0.4162	0.0443	0.4849	0.0065	2.1716	5959
4.0	0.3731	0.0553	0.4823	0.0079	2.7676	3951
5.0	0.3394	0.0598	0.4808	0.0088	3.3091	3206
6.0	0.3127	0.0631	0.4786	0.0100	3.6696	2475
7.0	0.2914	0.0641	0.4762	0.0123	4.0080	1695
8.0	0.2754	0.0626	0.4742	0.0139	4.3874	1313
9.0	0.2658	0.0613	0.4737	0.0148	4.6636	1131
10.0	0.2605	0.0605	0.4738	0.0154	4.8299	1048
11.0	0.2569	0.0613	0.4742	0.0162	4.8445	951
12.0	0.2531	0.0617	0.4743	0.0175	4.8728	814
13.0	0.2495	0.0623	0.4743	0.0197	4.8643	644
14.0	0.2465	0.0628	0.4737	0.0216	4.8385	532
15.0	0.2469	0.0633	0.4734	0.0233	4.7475	460
16.0	0.2481	0.0632	0.4734	0.0248	4.6945	405
17.0	0.2490	0.0654	0.4734	0.0263	4.5029	360
18.0	0.2485	0.0664	0.4728	0.0281	4.4026	317
19.0	0.2485	0.0678	0.4722	0.0297	4.2756	282
20.0	0.2481	0.0683	0.4718	0.0312	4.2148	255
21.0	0.2462	0.0683	0.4713	0.0326	4.2064	234
22.0	0.2450	0.0693	0.4706	0.0339	4.1345	217
23.0	0.2439	0.0700	0.4700	0.0352	4.0804	201
24.0	0.2430	0.0719	0.4694	0.0365	3.9712	187
25.0	0.2432	0.0733	0.4688	0.0380	3.8640	173

Table C.1 – Decidability of the 'LEI-a' data set with various centre wavelengths using just one filter, with sigmaOnF of 0.75 with a template size of 20x240, and 3 shifts.

λ_{min}	μ_s	σ_s	μ_d	σ_d	d`	DOF
2.0	0.4100	0.0432	0.4867	0.0051	2.4932	9477
3.0	0.3747	0.0490	0.4859	0.0056	3.1858	7940
4.0	0.3439	0.0542	0.4846	0.0065	3.6443	5965
5.0	0.3201	0.0575	0.4836	0.0076	3.9840	4337
6.0	0.3002	0.0582	0.4827	0.0086	4.3870	3342
7.0	0.2867	0.0587	0.4823	0.0096	4.6530	2712
8.0	0.2754	0.0590	0.4820	0.0104	4.8802	2324
9.0	0.2663	0.0587	0.4817	0.0111	5.1018	2021
10.0	0.2590	0.0590	0.4815	0.0121	5.2284	1703
11.0	0.2531	0.0587	0.4813	0.0131	5.3653	1460
12.0	0.2487	0.0589	0.4810	0.0140	5.4292	1272
13.0	0.2448	0.0601	0.4806	0.0150	5.3850	1126
14.0	0.2419	0.0604	0.4802	0.0157	5.4015	1011
15.0	0.2394	0.0612	0.4798	0.0167	5.3588	897
16.0	0.2372	0.0610	0.4794	0.0179	5.3854	781
17.0	0.2357	0.0615	0.4789	0.0190	5.3460	691
18.0	0.2348	0.0618	0.4784	0.0202	5.3015	613
19.0	0.2335	0.0626	0.4780	0.0214	5.2262	547
20.0	0.2323	0.0631	0.4775	0.0225	5.1756	492
21.0	0.2313	0.0634	0.4770	0.0238	5.1299	442
22.0	0.2309	0.0640	0.4765	0.0249	5.0560	404
23.0	0.2304	0.0646	0.4759	0.0260	4.9833	369
24.0	0.2300	0.0650	0.4754	0.0272	4.9263	338
25.0	0.2296	0.0651	0.4750	0.0284	4.8853	310

Table C.2 – Decidability of the 'LEI-a' data set with various centre wavelengths using just one filter, with sigmaOnF of 0.5 with a template size of 20x240, and 3 shifts.

λ_{min}	μ_s	σ_s	μ_d	σ_d	d`	DOF
2.0	0.3514	0.0502	0.4856	0.0061	3.7525	6721
3.0	0.3278	0.0522	0.4847	0.0070	4.2151	5042
4.0	0.3103	0.0534	0.4842	0.0081	4.5479	3818
5.0	0.2966	0.0543	0.4836	0.0092	4.8023	2965
6.0	0.2866	0.0554	0.4831	0.0101	4.9345	2437
7.0	0.2777	0.0558	0.4825	0.0111	5.0946	2016
8.0	0.2708	0.0565	0.4820	0.0122	5.1697	1689
9.0	0.2647	0.0568	0.4813	0.0132	5.2570	1443
10.0	0.2596	0.0572	0.4810	0.0145	5.3077	1193
11.0	0.2549	0.0574	0.4804	0.0155	5.3632	1033
12.0	0.2514	0.0572	0.4799	0.0168	5.4180	880

13.0	0.2485	0.0575	0.4794	0.0181	5.4138	759
14.0	0.2461	0.0579	0.4790	0.0195	5.3884	657
15.0	0.2442	0.0588	0.4785	0.0208	5.3115	576
16.0	0.2422	0.0592	0.4781	0.0222	5.2713	504
17.0	0.2409	0.0597	0.4776	0.0236	5.2153	446
18.0	0.2400	0.0603	0.4767	0.0251	5.1334	396
19.0	0.2390	0.0612	0.4765	0.0266	5.0355	351
20.0	0.2382	0.0622	0.4760	0.0281	4.9283	316
21.0	0.2380	0.0627	0.4755	0.0296	4.8452	285
22.0	0.2377	0.0632	0.4748	0.0310	4.7623	259
23.0	0.2378	0.0636	0.4745	0.0326	4.6827	235
24.0	0.2383	0.0643	0.4740	0.0340	4.5857	216
25.0	0.2383	0.0651	0.4734	0.0355	4.4823	198

Table C.3 - Decidability of the 'LEI-a' data set with various centre wavelengths using just one filter, with sigmaOnF of 0.3 with a template size of 20x240, and 3 shifts.

λ_{min}	μ_s	σ_s	μ_d	σ_d	d`	DOF
4.0	0.4301	0.0358	0.4785	0.0066	1.8787	5776
8.0	0.3453	0.0431	0.4731	0.0097	4.0938	2647
12.0	0.3109	0.0399	0.4759	0.0093	5.6981	2914
13.0	0.3053	0.0399	0.4750	0.0099	5.8397	2550
14.0	0.3006	0.0398	0.4742	0.0106	5.9642	2235
15.0	0.2966	0.0396	0.4734	0.0113	6.0674	1962
16.0	0.2931	0.0396	0.4725	0.0120	6.1344	1723
17.0	0.2903	0.0395	0.4715	0.0128	6.1736	1518
18.0	0.2877	0.0394	0.4705	0.0136	6.1987	1342
19.0	0.2853	0.0396	0.4694	0.0145	6.1748	1186
20.0	0.2832	0.0399	0.4683	0.0154	6.1206	1045
21.0	0.2812	0.0401	0.4671	0.0164	6.0660	925

Table C.4 – Different filter parameters using 'CASIA-a' with one filter with sigmaonf of 0.5, template size 20x240, 8 shifts L & R

#Shifts L&R	μ_s	σ_s	μ_d	σ_d	d`	DOF
0	0.3047	0.0914	0.4992	0.0184	2.9489	738
1	0.2654	0.0706	0.4918	0.0173	4.4019	835
2	0.2511	0.0608	0.4856	0.0153	5.2860	1060
3	0.2487	0.0589	0.4810	0.0140	5.4292	1272
4	0.2487	0.0589	0.4777	0.0132	5.3679	1427
5	0.2487	0.0589	0.4750	0.0128	5.3148	1533
6	0.2487	0.0589	0.4730	0.0123	5.2750	1640

7	0.2487	0.0589	0.4716	0.0120	5.2479	1739
8	0.2487	0.0589	0.4705	0.0117	5.2276	1817
9	0.2487	0.0589	0.4697	0.0116	5.2090	1851
10	0.2487	0.0589	0.4690	0.0115	5.1933	1879

Table C.5 – Effect of shifts with the 'LEI-a' data set.

#Shifts L&R	μ_s	σ_s	μ_d	σ_d	d`	DOF
0	0.3602	0.0731	0.4993	0.0153	2.6345	1061
1	0.3352	0.0611	0.4930	0.0142	3.5576	1240
2	0.3213	0.0520	0.4888	0.0128	4.4253	1524
3	0.3184	0.0502	0.4849	0.0112	4.5780	1991
4	0.3150	0.0431	0.4828	0.0108	5.3473	2152
5	0.3145	0.0427	0.4803	0.0099	5.3494	2547
6	0.3134	0.0403	0.4793	0.0096	5.6652	2684
7	0.3133	0.0399	0.4784	0.0094	5.6959	2824
8	0.3130	0.0397	0.4771	0.0091	5.7043	2989
9	0.3130	0.0397	0.4713	0.0090	5.4994	3076
10	0.3130	0.0397	0.4757	0.0089	5.6607	3124

Table C.6 – Effect of shifts with the 'CASIA-a' data set.